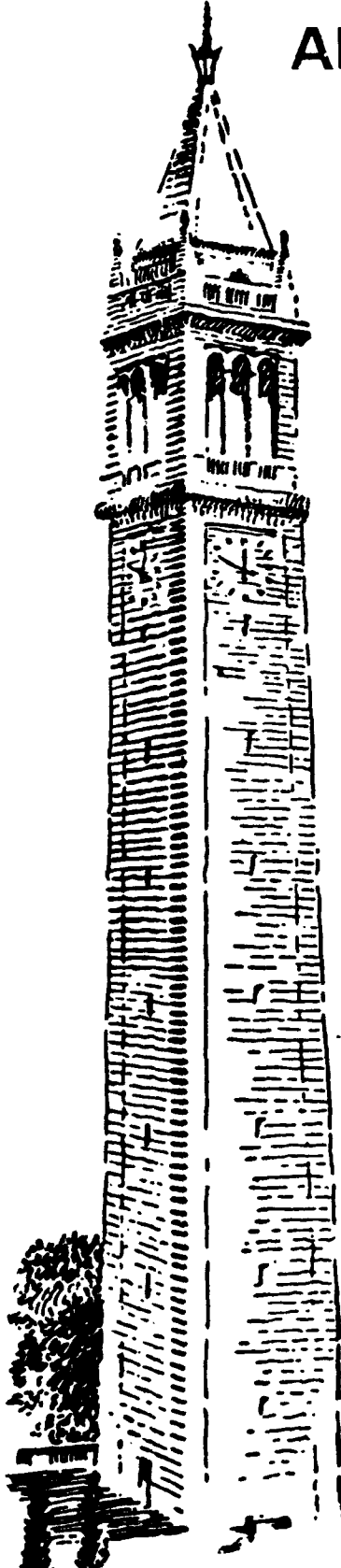


AD-A247 847

DTK

(2)



EVIDENCE OF STOCHASTIC DIFFUSION
ACROSS A CROSS-FIELD SHEATH DUE
TO KELVIN-HELMHOLTZ VORTICES

by

S. E. Parker, X. Q. Xu, A. J. Lichtenberg,
and C. K. Birdsall

Memorandum No. UCB/ERL M91/79

30 September 1991

92-02736



ELECTRONICS RESEARCH LABORATORY
College of Engineering
University of California, Berkeley, CA 94720

Statement A per telecon
Dr. Charles Roberson ONR/Code 1112
Arlington, VA 22217-5000

NWW 3/23/92

**EVIDENCE OF STOCHASTIC DIFFUSION
ACROSS A CROSS-FIELD SHEATH DUE
TO KELVIN-HELMHOLTZ VORTICES**

by

S. E. Parker, X. Q. Xu, A. J. Lichtenberg,
and C. K. Birdsall

N00014-89-J-1097

N00014-90-J-1198

Memorandum No. UCB/ERL M91/79

30 September 1991

ELECTRONICS RESEARCH LABORATORY

College of Engineering
University of California, Berkeley
94720

Evidence of Stochastic Diffusion across a Cross-Field Sheath due to Kelvin-Helmholtz Vortices

S. E. Parker[†], X.Q. Xu, A.J. Lichtenberg and C.K. Birdsall

Electronics Research Laboratory

University of California, Berkeley, California 94720

October 9, 1991

Abstract

We identify mechanisms for particle transport across a cross-field sheath. We present a study of $\mathbf{E} \times \mathbf{B}$ drift motion in a vortex in which the ion drifts are perturbed by their finite gyroradii and electron drifts are perturbed by one or more traveling waves. Large scale vortices, which are the result of nonlinear saturation of the Kelvin-Helmholtz instability resulting from shear in the $\mathbf{E} \times \mathbf{B}$ drift velocity, have been observed in plasma simulations of the cross-field sheath¹⁻³. Small scale turbulence is also present, and ions and electrons are transported across the sheath. A vortex alone does not allow for

[†]Present address: Plasma Physics Laboratory, Princeton University, Princeton, New Jersey 08543.

the observed electron transport because the electron drift orbits simply circulate. On the other hand, the ion motion can be stochastic from resonant interaction between harmonics of the the drift motion and the gyromotion, independent of the background turbulence. The fluctuations in the ion density would then give rise to small amplitude wave spectrum. The combined action of the vortex fields and traveling wave fields on the electron motion can then lead to stochastic electron diffusion. We study these effects, showing that the values of vortex fields observed in the simulation are sufficient to lead to both ion and electron stochasticity. Furthermore, the rate of the the resulting diffusion is sufficient to account for the diffusion observed in the simulation.

1 Introduction

In previous studies of the cross-field sheath, the Kelvin-Helmholtz (K-H) instability is found to saturate into large scale vortices, and in addition to the circular vortex flow, there is a bigger amplitude, small scale turbulence¹⁻³. The driving mechanism for the K-H instability is the $\mathbf{E} \times \mathbf{B}$ sheared flow that occurs due to nonuniform electric fields in the sheath near a conducting, absorbing wall. With the magnetic field taken parallel to the wall, the electric field is due to the weaker magnetization of the ions relative to the electrons, causing a net positive wall charge. This electric field is nonuniform (large at the wall, becoming small in the plasma), which causes a significant velocity shear; the mean velocity is $v_0 \sim \frac{1}{2}v_{Ti}$, where

v_{Ti} is the ion thermal velocity, and the shear length is $L_s \sim 5\rho_i$, where ρ_i is the thermal ion gyroradius. A characterization of the physical system is shown in Figure 1. Our objective in this paper is to understand how the vortices observed in the previous Refs. 1-3 can provide mechanisms for transport. The calculation presented here may be relevant to K-H vortices driven by other mechanisms as well.^{4,5}

There has been considerable research on chaotic single particle motion in plasmas, in which chaos in phase space has been generated by the resonant interaction of the particle gyration with magnetic field spatial periodicities^{6,7}, with periodic time varying fields^{8,9}, and with waves^{10,11}. The resonant mechanism for the generation of the stochasticity and the resulting particle diffusion is the overlap of neighboring harmonic resonances in the action space as reviewed in Refs. 12 and 13. There has also been interest in stochastic $\mathbf{E} \times \mathbf{B}$ motion and its role in transport due to drift waves both when the stochasticity is caused by an interaction of one or two waves¹⁴⁻¹⁶ or when the wave spectrum itself is turbulent^{17,18,19}. Our work is in the same spirit as Refs. 14-16, but our physical system, and associated Hamiltonian are quite different.

We postulate that the basic driving mechanism for the transport is the following. The nonlinear $\mathbf{E} \times \mathbf{B}$ motion within the vortices generate harmonics of the vortex frequency that resonate with the ion gyrofrequency. These harmonic resonances generate secondary

resonances whose interaction make the ion motion stochastic. The resulting interception of ion orbits by the walls leads to macroscopic charge fluctuations that generate a wave spectrum. The waves, in turn have frequencies that resonate with the $\mathbf{E} \times \mathbf{B}$ drift frequency of the vortex motion of the electrons to produce stochasticity and therefore electron diffusion. The sheath physics is therefore of key importance in setting up a nonuniform electric field, which leads to vortex flow and therefore a frequency spectrum associated with the vortex motion.

Although the driving terms for generating the stochasticity proceed from ions to electrons, the electron dynamics are easier to treat, so we reverse the order of presentation. In Part I, we concentrate on the electron $\mathbf{E} \times \mathbf{B}$ motion, which is also applicable to the zero order ion drift motion. In Section 2, we develop the interaction equations between an applied vortex field and one or more wave fields. In Section 3, we study orbits obtained from numerical integration of the equations of motion. We show results using single and multiple waves, and compare with the analytic predictions. We also show the importance of the edge velocity shear. In Section 4, using a resonance overlap criterion, we calculate how large the perturbing wave needs to be to cause large scale stochasticity.

In Part II we consider the interaction of the finite ion gyromotion with the vortex. In Section 5, we introduce the interaction Hamiltonian and the appropriate transformations.

The numerical interactions and comparison with theory are presented in Section 6. In Section 7 we again use the overlap criterion to determine the parameter region for large scale stochasticity. In Section 8 we calculate and measure the diffusion coefficient arising from the ion stochastic motion, and compare it to a simulation of the ion motion in a applied vortex field.

We emphasize that these calculations are not self-consistent as both the vortex field and the wave field are imposed. However, the amplitudes of those fields are taken from the self-consistent simulations, and the results of the calculations show electron and ion diffusion consistent with the observed self-consistent diffusion. Thus, we believe that these calculations uncover the mechanisms operating to produce the self-consistent diffusion.

Part I

2 Electron Drift Motion Interacting with Traveling Waves

In all calculations we will use the configuration specified in Refs. 1-3 which is given in Figure 1. The magnetic field \mathbf{B} is constant and perpendicular to the x-y plane (parallel to the wall), and the electric field \mathbf{E} is in the x-y plane. We assume that the time dependent variation of the electric field is much smaller than the electron cyclotron frequency ($\omega \ll \omega_{ce}$). In Part I

we also assume that all the field spatial scale lengths are much bigger than the electron gyroradius ($\frac{\nabla E}{E} \rho_e \ll 1$). Hence, in this section we can use the zero order drift equation for the motion of the electrons

$$\mathbf{v} = \frac{\mathbf{E} \times \mathbf{B}}{B^2}. \quad (1)$$

This is also applicable to the zero order ion drift motion. However, as will be discussed in Part II, finite gyroradius and gyrofrequency effects are also important for ion motion in the vortex. Written out in component form, in terms of the potential defined by $\mathbf{E} = -\nabla\Phi$, we see that Eq. (1) is in Hamiltonian form with x being the canonical momentum and y the position,

$$\dot{x} = -\frac{1}{B} \frac{\partial \Phi}{\partial y}, \quad (2)$$

$$\dot{y} = \frac{1}{B} \frac{\partial \Phi}{\partial x}. \quad (3)$$

where Φ plays the part of the system Hamiltonian. For Φ independent of time, the particles follow the equipotential contours $\Phi(x, y) = \Phi[x(t=0), y(t=0)]$.

We now study the particle motion in a time dependent electrostatic potential given by

$$\begin{aligned} \Phi(x, y, t) = & -B v_0 \left(x - \frac{x^2}{2L_s} \right) - \Phi_0 \psi \left[\left(\frac{x}{\alpha \rho_i} \right)^2 + \left(\frac{y + v_0 t}{\beta \rho_i} \right)^2 \right] \\ & + \epsilon \Phi_0 \sum_n A_n e^{i(k_n y - \omega_n t)}, \end{aligned} \quad (4)$$

where v_0 is the drift velocity of the vortex and L_s is the velocity shear length. The potential

has a magnitude Φ_0 and a “shape function” ψ specifying the shape of the vortex equipotentials that specifies the vortex flow; α and β specify the elongation in the x, y directions. Defining $\gamma = \frac{\epsilon\Phi_0}{T_i}$, then γ and ϵ are dimensionless parameters specifying the strengths of the vortex and waves, respectively. The elliptical shape for the zero order contours in Eq. (4) was assumed: (1) because of reasonable comparison with results^{2,3}; (2) for clarity and ease of the calculations. The results presented below can be used for other closed contour shapes. A contour plot of Eq. (4) is shown in Figure 2 with Gaussian $\psi(u) = e^{-\frac{1}{2}u^2}$, with $B = 1$, and the dimensionless parameters the same as used in the simulation^{2,3} $\gamma = 2.5$, $\alpha = 1.25$, $\beta = 3.83$, $v_0 = 0.44v_{Ti}$, $\rho_i/L_s = 0.8$, and $k\rho_i = 3.83$. We note that in the simulations ρ_i and v_{ti} are routinely set equal to one, such that the dimensionless quantities here correspond to the quantities in the simulation.

The notation can be simplified by making the following coordinate transformation to dimensionless coordinates in a frame moving with the vortex

$$\begin{aligned}\bar{x} &= \frac{x}{\alpha\rho_i}, \\ \bar{y} &= \frac{y + v_o t}{\beta\rho_i}, \\ \bar{t} &= \frac{\gamma\Omega t}{\alpha\beta}, \\ \bar{\Phi} &= \frac{\Phi}{\Phi_0},\end{aligned}$$

where Ω is the thermal ion gyrofrequency. Dropping the overbars for notational convenience,

the equations of motion are now

$$\dot{x} = -\frac{\partial \Phi}{\partial y}, \quad (5)$$

$$\dot{y} = \frac{\partial \Phi}{\partial x}. \quad (6)$$

with the transformed Hamiltonian

$$\Phi(x, y, t) = -\psi(x^2 + y^2) + \delta x^2 + \epsilon \sum_n A_n e^{i(\tilde{k}_n y - \tilde{\omega}_n t)}. \quad (7)$$

where $\delta = \frac{\alpha^2 v_o \rho_i}{2\gamma v_{Ti} L_s}$, parameterizes the amount of velocity shear. We will assume δ small;

using the early values produces $\delta \simeq 0.1$. The transformed \tilde{k} , $\tilde{\omega}$ in terms of the laboratory frame k , ω , are

$$\tilde{k}_n = \beta k_n \rho_i, \quad (8)$$

$$\tilde{\omega}_n = \frac{\alpha \beta}{\gamma} \Omega^{-1} (\omega_n + k_n v_0). \quad (9)$$

Next, we make the transformation from (x, y) coordinates to their corresponding action-angle coordinates (J, θ) , using the partial generating function

$$F_1(y, \theta_0) = \frac{1}{2} y^2 \cot \theta_0. \quad (10)$$

The new and old variables are related by

$$x = \frac{\partial F_1}{\partial y}, \quad (11)$$

$$J_0 = -\frac{\partial F_1}{\partial \theta_0}, \quad (12)$$

which after rearranging gives

$$x = \sqrt{2J_0} \cos \theta_0, \quad (13)$$

$$y = \sqrt{2J_0} \sin \theta_0. \quad (14)$$

For drift motion in a quadratic well, J_0 gives the area, divided by 2π , inside the curves of constant Hamiltonian, and θ_0 is a uniformly rotating angle. Defining the unchanged wave phases

$$\theta_n = \bar{\omega}_n t, \quad n = 1, 2, 3, \dots, N. \quad (15)$$

It is necessary to increase the system's degrees of freedom to keep the angle variables periodic. We have assumed the waves are independent (no harmonics). We now obtain the Hamiltonian $H = H_0 + \epsilon H_1$,

$$H_0(J_0, J_1, J_2, \dots, J_N) = -\psi(2J_0) + \sum_{n=1}^{n=N} \bar{\omega}_n J_n, \quad (16)$$

$$H_1(J_0, \theta_0, \theta_1, \theta_2, \dots, \theta_N) = \frac{\delta}{\epsilon} 2J_0 \cos^2 \theta_0 + \sum_{n=1}^{N} A_n \sum_{l=-\infty}^{l=\infty} J_l^B(\bar{k}_n \sqrt{2J_0}) e^{i(l\theta_0 - \theta_n)}, \quad (17)$$

where J_l^B are Bessel functions of integer order, which arise from the expansion of (14) in the exponent^{12,13}. From this form, it is seen that each wave adds one degree of freedom to the system, but a single wave generates an infinite set of resonances between harmonics of

the drift frequency and harmonics of the wave frequencies. The second term in Eq. (16) preserves the canonical form for $n \geq 1$. Eqs. (13)-(17) make no reference to the assumed shape of the vortex contours, beyond the form indicated in (7). Hence, the results here and following can be generalized to other vortex shapes satisfying this form. In a general case J_0 would be the area inside the closed contour of the potential divided by 2π (with ϵ set to zero)¹⁶.

For ϵ equal to zero, J_0 is a constant of motion and the drift frequency around the vortex $\tilde{\omega}_d$ is defined by:

$$\tilde{\omega}_d = \dot{\theta}_0 = \frac{\partial \psi(2J_0)}{\partial J_0}. \quad (18)$$

For small ϵ , we expect resonances when $l\tilde{\omega}_d = m\tilde{\omega}_n$, where l, m are integers. If ψ is nonlinear, which is the case of interest, then $\tilde{\omega}_d$ is a function of J_0 and there will be many resonances for a given $\tilde{\omega}_n$. These resonances generate islands in the phase space which can overlap to provide a mechanism for an electron to stochastically change J_0 , hence providing a mechanism for transport^{6,13}.

3 Numerical Results for $E \times B$ Motion

In the K-H simulations, small amplitude and short scale waves traveling in the y -direction were observed throughout the simulation ($\epsilon \ll 1$, $k\rho_i \sim 1$ and $\frac{w}{\lambda} \sim 1$). In this section we

show how the short wavelength and small amplitude waves can provide a mechanism for transport. We add a small amplitude wave component to the large scale vortex flow and study the resulting $\mathbf{E} \times \mathbf{B}$ particle motion. A single wave of appropriate amplitude should be sufficient to obtain global stochasticity and we concentrate on this case. We again choose:

$\psi(u) = -e^{-\frac{1}{2}u}$, and we neglect velocity shear ($\delta = 0$). The potential is then

$$\Phi(x, y, t) = -\exp\left(-\frac{1}{2}(x^2 + y^2)\right) + \epsilon \cos(\tilde{k}y - \tilde{\omega}t) \quad (19)$$

In this case, with $\epsilon = 0$, the drift frequency is: $\omega_d = \exp(-J_0)$. The values for α , β , and γ are approximately 1.25, 3.83 and 2.5 for the simulation presented in Refs. [2,3]. In the normalized units the maximum drift frequency is: $\tilde{\omega}_{b,max} = 1$, which in the laboratory units is: $\omega_{b,max} = \left(\frac{\gamma\Omega}{\alpha\beta}\right) \tilde{\omega}_{b,max} \approx 0.52\Omega$. This compares reasonably well to the observed value of 0.5Ω [3].

We integrate the equations of motion Eq. (5) and (6), for a set of orbits using the classical fourth order Runge-Kutta method²⁰. The wave potential is given by Eq. (19) with $\tilde{k} = 3.83$, $\tilde{\omega} = 0.96$. Our choice of $\tilde{k}, \tilde{\omega}$ was made so that $k\rho_i = 1$ and ω was a representative point from the power spectrum at $k\rho_i \approx 1$. Fig. 8 in Ref. 3 shows the power spectrum peaked at $\omega_0 \approx -kv_0$, where $v_0 \approx 0.44v_{Ti}$, but is fairly broad at $k\rho_i \approx 1$ with a range between $-2\omega_0$ and zero. In Figure 3 we display integrations from a set of initial locations: $x_i(t=0) = 0.05i$ and $y_i(t=0) = 0$ with $i = 1, 2, \dots, 20$. Surface of section plots in (x, y) are

shown for 1000 periods of the perturbing wave (so that there are 20,000 total points). The surface of section is defined at constant phase of the wave variable, i.e., when $\omega t = 2n\pi$, where n integer. If a constant of the motion exists, then it has been generally shown¹³ that x and y will lie on a smooth curve in this surface. If the constant does not exist, then the trajectory can puncture the surface of section over a two-dimensional area.

We observe the transition between these two types of behavior in Figs. 3(a) and 3(b). The plots show the change in character as ϵ is varied over a range consistent with the wave amplitudes observed in the simulation. (a) $\epsilon = 0.015$, and (b) $\epsilon = 0.02$. In Fig. 3(a) the motion is mainly confined to smooth curves or bounded in small areas between smooth curves. The latter regions develop near the separatrices of island chains formed by resonances between the drift motion around the vortex and the drift motion in the wave field. In these bounded separatrix layers the constant of the motion does not exist, but this has little effect on the overall dynamics. In Fig. 3(b), the separatrix layers of neighboring islands have overlapped to make a broad layer of stochasticity. This is clearly seen in the escape of trajectories to much larger values of the coordinates. If trajectories intersect sources and sinks of plasma they would then result in diffusion. We present a quantitative calculation of diffusion in the next section. Figure 4 is the surface of section plots using the action-angle coordinates (J_0, θ_0) for the $\epsilon = 0.015$ case.

If we consider that more than one wave is in the perturbing field, the potential would have the following form

$$\Phi(x, y, t) = -\exp \left\{ -\frac{1}{2}(x^2 + y^2) \right\} + \epsilon \sum_{m=1}^M A_m \cos(\tilde{k}_m - \tilde{\omega}_m t + \Theta_m), \quad (20)$$

We would expect that, for the same overall wave amplitude level, phase decorrelations might increase the level of stochasticity. As an example, we use four waves ($N = 4$), two with positive $\tilde{\omega}$, two with negative $\tilde{\omega}$, all having $k\rho_i = 1.024$, and the amplitudes representative of the power spectrum given in Ref. 3, Figure 8. The phases Θ_m were chosen to be random. The parameters used for the four waves $n = (1, 2, 3, 4)$ are: $\tilde{k}_n = 4.16$, $\tilde{\omega}_n = (-0.6, -0.3, 0.4, 0.7)$, $\epsilon A_n = (0.004, 0.006, 0.01, 0.012)$, and $\Theta_m = (1.1, 5.5, 3.0, 0.0)$. Figure 5 shows a surface of section plot, where points are plotted when $\tilde{\omega}_4 t = m2\pi$, $m = 0, 1, 2, 3, \dots$. This surface of section is chosen because mode four has the largest amplitude, so that residual structure can still be seen. The lack of a true surface of section in which to see regular motion prevents a quantitative comparison with the single wave case, but the impression is of increasing stochasticity with more than one wave.

We can also investigate the role velocity shear plays in the $\mathbf{E} \times \mathbf{B}$ particle motion. We do this by adding δx^2 to Eq. (19). The velocity shear permits plasma to flow past and interact with the vortex. This type of shear is observed in the self-consistent simulations. The velocity is strongest at the wall and drops off to zero towards the center of the plasma.

The form x^2 used for modeling the shear only applies up to $x = 2L_s/(\alpha\rho_i)$, at which point the drift velocity goes to zero, as can be seen from Eq. (4). The velocity shear and vortex provide a “snow shovel” mechanism, by which the vortex drifts along the wall and scrapes off interior plasma which is within the reach of the vortex ($\sim 5\rho_i$). This mechanism is shown in Figure 6, using the example of $\epsilon = 0.03$, an $\delta = 0.015$ for a single wave. Four test particle orbits are shown just at the edge of the vortex.

4 Island Formation and Overlap Criterion for Global Stochasticity

We begin by studying a single wave. To find out for what range of parameters global (large scale) stochasticity occurs, we calculate the overlap of the first two integer resonances: $\tilde{\omega}_d = \tilde{\omega}/m$, $m=1,2$. These two resonances are chosen because we are interested in waves with $\tilde{\omega} \lesssim \omega_{d,max}$, and these are the primary resonances observed in the simulation results presented in Section 3. We make a transformation to the slowly varying phase close to resonance: $\phi_0 = m\theta_0 - \theta_1$, and the fast phase of interest: $\phi_1 = \theta_1/m$. Using the generating function:

$$F_2(I_0, I_1; \theta_0, \theta_1) = (m\theta_0 - \theta_1)I_0 + \theta_1 I_1/m,$$

we obtain:

$$I_0 = J_0/m, \quad (21)$$

$$I_1 = J_0 + mJ_1,$$

$$\phi_0 = m\theta_0 - \theta_1,$$

$$\phi_1 = \theta_1/m.$$

Which explicitly exhibits the slow phase ϕ_0 . The new Hamiltonian is then $H = H_0 + \epsilon H_1$

where

$$H_0(I_0, I_1) = -\psi(2mI_0) + \tilde{\omega}(I_1/m - I_0), \quad (22)$$

$$\begin{aligned} H_1(I_0, \theta_0, \theta_1) &= \frac{\delta}{\epsilon} 2mI_0 \cos^2(\phi_0/m + \phi_1) \\ &+ \epsilon \sum_{l=-\infty}^{l=+\infty} J_l^B(\tilde{k}\sqrt{2mI_0}) e^{i(\frac{l}{m}\phi_0 + (l-m)\phi_1)}, \end{aligned} \quad (23)$$

and we have taken $A_1 = 1$. Next, we average over the fast phase ϕ_1 to obtain:

$$\bar{H} = -\psi(2mI_0) - \tilde{\omega}I_0 + \delta mI_0 + \epsilon J_m^B(\tilde{k}\sqrt{2mI_0}) e^{i\phi_0} \quad (24)$$

where: $\bar{H} = \frac{1}{2\pi} \int_0^{2\pi} H d\phi_1$. At this point we drop the zero subscript since the the phase

averaged system is now one dimensional. Setting $\frac{\partial \bar{H}}{\partial I} = 0$, $\frac{\partial \bar{H}}{\partial \phi} = 0$, gives the fixed points,

which are

$$I_{fp} = \frac{1}{2m} [\psi']^{-1}(-\tilde{\omega}/2m), \quad (25)$$

$$\phi_{fp1,2} = (0, \pi), \quad (26)$$

where we have neglected terms of order ϵ in determining I_{fp} . We can then expand $I = I_{fp} + \Delta I$ to obtain¹³:

$$\Delta H = G \frac{\Delta I^2}{2} - F \cos \phi \quad (27)$$

where $G = 4m^2\psi''(2mI_{fp})$, $F = -\epsilon J_m^B(\tilde{k}\sqrt{2mI_{fp}})$. The maximum ΔI is

$$\Delta I_{max} = 2\sqrt{\frac{F}{G}} = \left[\frac{-\epsilon J_m^B(\tilde{k}\sqrt{2mI_{fp}})}{m^2\psi''(2mI_{fp})} \right]^{1/2}. \quad (28)$$

As an estimate of the onset of large scale stochasticity we use the “two-thirds rule”, which corresponds to the destruction of the last KAM surface between islands(at $K=1$ for the standard map)¹³:

$$\frac{\Delta I_{max}(m=1) + \Delta I_{max}(m=2)}{I_{fp}(m=2) - I_{fp}(m=1)} \geq \frac{2}{3} \quad (29)$$

To proceed further the vortex shape ψ needs to be specified. We use

$$\psi(u) = e^{-\frac{1}{2}u}, \quad (30)$$

which gives a qualitative fit to the vortex observed in Refs. 2 and 3. Using this shape we calculate the location of the m th resonance in action space to be at

$$I_{fp} = -\frac{1}{m} \ln(\bar{\omega}/m). \quad (31)$$

Using (30) to calculate ψ'' in (28), the approximate width of the m th resonance is

$$\Delta I_{max} = 2 \left[\frac{\epsilon J_m^B(\tilde{k}\sqrt{2mI_{fp}})}{m\bar{\omega}} \right]^{1/2}. \quad (32)$$

We can now use Eq. (29) with Eqs. (31) and (32) to calculate the critical value for the perturbation strength:

$$\epsilon_c = \frac{(\ln 2\bar{\omega})^2}{36} \bar{\omega} \left\{ \sqrt{J_1^B \left[\tilde{k} \sqrt{-2 \ln(\bar{\omega})} \right]} + \sqrt{\frac{1}{2} J_2^B \left[\tilde{k} \sqrt{-2 \ln(\bar{\omega}/2)} \right]} \right\}^{-2}. \quad (33)$$

The value of ϵ_c gives an estimate of the strength of the background perturbing wave which is needed to cause large scale stochasticity. The predicted critical value for the perturbation strength obtained using Eq. (33) is: $\epsilon_c = 0.012$, which is in reasonable agreement with the numerical results which show the transition to large stochasticity occurring between Figs. 3(a) and 3(b). If we assume that ϵ is sufficiently large that the resonance islands strongly overlap, i.e. (29) is well satisfied, there is good mixing of the particles in the vortex and we can then estimate the stochastic diffusion coefficient by its quasilinear value

$$D_s \simeq \Delta L^2 \frac{\Omega_D}{2\pi} \quad (34)$$

where Ω_D is the drift frequency and ΔL a characteristic diffusion distance in physical space expressed in dimensional units. We associate ΔL with the half island size, given in (32), where ΔL and ΔI_{max} are related through the transformation equations. Substituting Eqs. (32), (31) and (18) into (34) we obtain, in dimensional units

$$D_s \simeq \frac{2\gamma}{\pi} \sqrt{\epsilon J_m^B \left(\tilde{k} \sqrt{-2 \ln(\frac{\bar{\omega}}{m})} \right) \frac{\bar{\omega}}{m} \left(\frac{T_i}{eB} \right)}. \quad (35)$$

We note that the factor $\frac{T_i}{eB} = \rho_i^2 \Omega$ restore the dimensionality, but does not imply that D_s

has Bohm scaling, since the dimensionless factors can also change with this ratio. We will compare this result with the ion diffusion obtained in Sec II. From Eq. (35) we obtain the value of the stochastic diffusion coefficient is $D_s \simeq 0.07 \frac{T_i}{eB}$. It is worth pointing out that the similar issue has been addressed in a quite different system in which equilibrium and perturbed states are two dimensional periodic flows with perturbed flow propagating in y-direction.²¹

Part II

5 Interaction of the Ion Drift and Gyromotion

Because the gyro-orbits of the ions are comparable in size to the vortex, the drift approximation can no longer be used. Furthermore, the gyromotion adds a second degree of freedom which allows resonances even in the absence of a wave field. We now consider the formulation of the ion dynamics including the full gyro and drift motion.

In the uniform magnetic field $B_0\hat{z}$ from the vector potential $\vec{A}_0(y) = -B_0y\hat{x}$, the total Hamiltonian is

$$H = \frac{1}{2M}|p_x + eB_0y|^2 + \frac{1}{2M}p_y^2 + e\Phi(x, y, t). \quad (36)$$

with the electrostatic potential well

$$\Phi(x, y, t) = -B_0 v_0 x - \Phi_0 \psi \left[f \left(\frac{x}{\rho_i} \right) + g \left(\frac{y + v_0 t}{\rho_i} \right) \right]. \quad (37)$$

Here, v_0 is the drift velocity of the vortex, ψ , f and g are functions specifying the shape of the vortex. For analysis of ion motion, we concentrate on the motion inside a vortex potential well and therefore can neglect the velocity shear and the perturbed wave background in Eq. (37) in contrast to Eq. (4).

As in Part I, we eliminate t by transforming to the frame moving with the vortex velocity v_0 : $(x, y; p_x, p_y) \rightarrow (u, v; P_u, P_v)$, with new coordinates in dimensionless units:

$$\begin{aligned} u &= \frac{x}{\rho_i}, \\ v &= \frac{y + v_0 t}{\rho_i}, \\ P_u &= \frac{p_x}{M v_{Ti}} - \frac{v_0}{v_{Ti}} \Omega t, \\ P_v &= \frac{p_y}{M v_{Ti}} + \frac{v_0}{v_{Ti}}, \\ H &= \frac{H}{T_i}. \end{aligned}$$

Following the treatment of Smith and Kaufman,¹¹ we transform to guiding center coordinates (X, Y) and local polar gyrocoordinates (ρ, ϕ) , $(u, v; P_u, P_v) \rightarrow (Y, X; \phi, P_\phi)$, by

$$Y = v + \rho \sin \phi, \quad (38)$$

$$X = u - \rho \cos \phi,$$

$$\begin{aligned}\phi &= \tan^{-1}\left(\frac{P_u + v}{P_v}\right), \\ P_\phi &= \frac{1}{2}\rho^2 = \frac{1}{2}[(P_u + v)^2 + P_v^2].\end{aligned}$$

This transformation allows separation into fast gyromotion and slow drift motion so that we can use the method of averaging. The Hamiltonian is then

$$H = P_\phi - \gamma\psi[f(X + \rho \cos \phi) + g(Y - \rho \sin \phi)]. \quad (39)$$

As in Part I, we exhibit this structure by transforming to action-angle-like variables. We already have the pair (P_ϕ, ϕ) for the gyromotion. The transformation of the drift variables to (J, θ) follow as in (10). Choosing

$$\begin{aligned}X &= \sqrt{2J} \cos \theta, \\ Y &= \sqrt{2J} \sin \theta.\end{aligned} \quad (40)$$

which is equivalent to Eqs. (13,14). The Hamiltonian becomes:

$$H = P_\phi - \gamma\psi[f(\sqrt{2J} \cos \theta + \rho \cos \phi) + g(\sqrt{2J} \sin \theta - \rho \sin \phi)]. \quad (41)$$

6 Numerical Results for Ion Motion

In order to compare with 2d simulation results, we choose two forms of the potential well:

(a), as in Part I,

$$\gamma\psi(x, y) = \gamma \exp\left[-\frac{1}{2}\left(\frac{x^2}{\alpha^2 \rho_i^2} + \frac{y^2}{\beta^2 \rho_i^2}\right)\right] \quad (42)$$

which gives a qualitative fit to the vortex shape with $\gamma = 2.5$, $\alpha = 1.25$ and $\beta = 3.75$; and

(b),

$$\gamma\psi = \gamma\left[\left(\frac{x}{a\rho_i}\right)^2 - \xi\left(\frac{x}{a\rho_i}\right)^4 + \frac{1}{2}(1 - \cos\frac{\pi y}{b\rho_i})\right] \quad (43)$$

which gives a qualitative fit to the vortex shape out to the vortex separatrix with $a = 1.59$,

$b = 7.5$ and $\xi = 0.17$. This form allows an analytical calculation of the primary resonances of all harmonic numbers which we perform in Sec. 7. Figs. 7(a)-(b) plot a 3-d surface and contours of potential of Eq. (43).

The equations of motion

$$\begin{aligned} \frac{d\vec{v}}{dt} &= \frac{e}{m}(-\nabla\Phi + \vec{v} \times \vec{B}), \\ \frac{d\vec{x}}{dt} &= \vec{v}. \end{aligned} \quad (44)$$

which are integrated by a Boris mover.²² Since the Hamiltonian is independent of time, its numerical value has been checked and is essentially conserved during the integration.

In order that a surface of section exhibit nonintersecting orbits, we start with all particles having the same Hamiltonian and vary the initial particle positions and velocities. In Figs. 8 and 9 we display integration from a set of initial locations on the circle: $x_i = r_0\alpha \cos \phi_{0i}$, $y_i = r_0\beta \sin \phi_{0i}$, $v_{xi} = v_{00} \cos \theta_{0i}$, and $v_{yi} = v_{00} \sin \theta_{0i}$ with ϕ_{0i} and θ_{0i} uniformly distributed between 0 and 2π .

Because of the complexity of the orbits, we visualize the motion both by plotting a

particle trajectory in physical space and a number of trajectories in the surface of section. From the particle trajectory, we find the ratio of gyrofrequency Ω_c (where Ω_c is the individual particle gyrofrequency with a specific velocity) to the $\vec{E} \times \vec{B}$ drift frequency Ω_d and obtain a qualitative feeling for the dynamics. As in Part I, to determine if an orbit is chaotic or regular, we generate a two-dimensional surface of section, plotting guiding center coordinates Y vs X at a particular value of ϕ ($\phi = 0$ is convenient). This is accomplished numerically by solving the equations of motion in Cartesian coordinates and calculating v_x at each time step; when v_x changes sign (which is equivalent to $\phi = 0$), we calculate X and Y according to Eqs. (38).

We first demonstrate the effect of a resonance between a harmonic of the drift motion and gyromotion for potential form (a), illustrating the “divided phase space” of regular and stochastic orbits. Since the inflection point of the vortex has zero velocity shear, most of the particles in that neighborhood have small shear and therefore the resulting islands have large amplitude. We therefore take the inflection point $r_0 = 1.0$ as the initial position and $v_{00} = 0.71v_{Ti}$. Fig. 8(a) shows a primary 4:1 resonance between the gyrofrequency and drift frequency of a particle orbit in configuration space, clearly showing the resonance of four gyro-orbits to one drift orbit. Fig. 8(b) shows successive intersections of a number of trajectories with the surface of the section, with the orbit of Fig. 8(a) being one of

the regular (island) orbits. The upper boundary of the phase space is limited by energy conservation. The inner space is bounded by KAM curves.

The generic resonance features exist for various potential forms. Figs. 9(a)-(b) show the metamorphoses of the $Y - X$ surface of section with varying initial position r_0 and velocity v_{00} of the potential form (b). For fixed initial position $r_0 = 0.5$, Fig. 9(a) shows that, for $v_{00} = 1.55v_{Ti}$, the motion is regular with a 5-1 resonance inside the potential well and higher resonances near the separatrix. As we allow v_{00} to increase to $1.70v_{Ti}$, the islands become larger with the higher order islands overlapping to become a seed for stochastic orbits, developing into a stochastic layer surrounding the separatrix, as depicted in Fig. 9(b). If v_{00} is increased further, $v_{00} > 1.95v_{Ti}$, some orbits can wander out of the vortex cell and escape. If the initial particle velocities are high enough, then the motion near the center of the vortex can also be stochastic, as the particle gyroradii are sufficiently large to extend into the nonlinear part of the vortex potential. For the parameters chosen for potential (b), particle motion can be stochastic and escape if $v_{00} > 2.72v_{Ti}$ even with $r_0 = 0$ initially. From Figs. 9(a)-(b), we conclude that the motion becomes stochastic, spreading out from the separatrix as the velocity increases.

7 Formation of Islands and an Overlap Criterion

If the gyromotion and drift motion cannot be separated by averaging, resonances that are present in the Hamiltonian between gyromotion and harmonics of the drift motion become important. These resonances lead to islands in the phase space that have their own local phase space structure. Depending on the dynamics, these resonances may be well separated or close together. If closed together, then their overlap leads to bands of stochasticity resulting in diffusive motion across the vortex. If well separated, the stochasticity may develop by the interaction of second-order resonances. These resonances are between harmonics of the primary island oscillation and the fundamental drift frequency Ω_d . The analytical treatment of either type of resonance can be performed by the transformation to the resonant frame, as done in Part I. The new coordinates measure the slow oscillation of the variables about their values at resonance, which is an elliptic fixed point of the new phase plane.

In the following, we proceed as in previous section to obtain the motion near an elliptic singular point. We choose the potential well as

$$\psi = [(\frac{x}{a\rho_i})^2 - \xi(\frac{x}{a\rho_i})^4 + \frac{1}{2}(1 - \cos \frac{\pi y}{b\rho_i})]. \quad (45)$$

such that the cosine term has a simple analytic expansion to exhibit the infinite set of resonances. We transform to the action angle coordinates as in Eq. (40) and use the Bessel

function identity

$$\exp(ia \sin \phi) = \sum_{l=-\infty}^{\infty} J_l^B(a) \exp(il\phi), \quad (46)$$

to write the Hamiltonian in a form where the resonances are explicitly exhibited:

$$\begin{aligned} H &= P_\phi - \frac{\gamma}{a^2} \{ (\sqrt{2J} \cos \theta + \rho \cos \phi)^2 \\ &- \frac{\xi}{a^2} (\sqrt{2J} \cos \theta + \rho \cos \phi)^4 + \frac{a^2}{2} \} + \frac{\gamma}{4} \sum_{n=-\infty}^{\infty} \sum_{l=-\infty}^{\infty} \{ J_n^B(2\sqrt{2J}) J_l^B(-\frac{\pi\rho}{b}) \\ &+ J_n^B(-2\sqrt{2J}) J_l^B(\frac{\pi\rho}{b}) \} e^{i(n\theta+l\phi)}. \end{aligned} \quad (47)$$

Noting the property of the Bessel function $J_l^B(-x) = (-1)^l J_l^B(x)$ and $J_{-l}^B(x) = (-1)^l J_l^B(x)$

, we can conclude that the resonances only have significant amplitude when n and l are both odd or both even. The strongest primary resonance has the lowest order Bessel function for which $\Omega_c = m\Omega_d$. Keeping only $l = \pm 1$ and $n = \pm m$ terms (where m is odd) the Hamiltonian which describes the resonance is given by

$$\begin{aligned} H_r &= P_\phi - \frac{\gamma}{a^2} \{ (\sqrt{2J} \cos \theta + \rho \cos \phi)^2 \\ &- \frac{\xi}{a^4} (\sqrt{2J} \cos \theta + \rho \cos \phi)^4 + \frac{a^2}{2} \} - \frac{\gamma}{2} J_m^B(\frac{\pi}{b}\sqrt{2J}) J_1^B(\frac{\pi\rho}{b}) \cos(m\theta - \phi). \end{aligned} \quad (48)$$

Transforming to a slow variable near resonance by the generating function

$$F_2 = (m\theta - \phi)\hat{J} + \phi\hat{P}_\phi, \quad (49)$$

we have the new variables as in (21) for which the slow variable $\hat{\theta} = m\theta - \phi$ is explicitly exhibited.

Averaging over the rapidly varying angle $\hat{\phi}$, the Hamiltonian becomes

$$\begin{aligned}\bar{H} &= \tilde{\Omega}(\hat{P}_\phi - \hat{J}) - \frac{\gamma}{a^2}m\hat{J} + \frac{3\xi\gamma}{8a^4}(2m\hat{J})^2 - \frac{\gamma}{2} \\ &\quad - \frac{\gamma}{2}J_m^B\left(\frac{\pi}{b}\sqrt{2m\hat{J}}\right)J_1^B\left(\frac{\pi\rho}{\beta}\right)\cos\hat{\theta}\end{aligned}\quad (50)$$

where $\tilde{\Omega} = 1 - \frac{\gamma}{a^2}$ is the normalized gyrofrequency modified by the vortex potential, and we have assumed the distance from the center of the vortex to the fixed point $R = \sqrt{2m\hat{J}} \gg 1$.

The location of the fixed points $\hat{\theta}_{fp}, \hat{J}_{fp}$ are determined as in (25) and (26) at $\hat{\theta}_{fp} = 0, \pi$,

and

$$2m\hat{J}_{fp} = \frac{2a^2}{3\xi m}\left[m - 1 + \frac{a^2}{\gamma}\right]. \quad (51)$$

The island Hamiltonian about the fixed points J_{fp} is

$$\Delta\bar{H} = G(\hat{J}_{fp})\frac{(\Delta\hat{J})^2}{2} - F(\hat{J}_{fp})\cos\hat{\theta} \quad (52)$$

where

$$\begin{aligned}G(\hat{J}_{fp}) &= \frac{\partial^2\bar{H}}{\partial\hat{J}^2} = \frac{\xi\gamma}{a^4}\frac{3}{4}(2m)^2 \\ F(\hat{J}_{fp}) &= \frac{\gamma}{2}J_m^B\left(\frac{\pi}{b}\sqrt{2m\hat{J}_{fp}}\right)J_1^B\left(\frac{\pi\rho}{b}\right)\end{aligned}\quad (53)$$

The island frequency near the stable point is now

$$\Omega_I = \sqrt{F(\hat{J}_{fp})G(\hat{J}_{fp})} = \Omega_d \frac{mb}{\pi a} \left\{ \frac{3\xi}{2} J_m^B\left(\frac{\pi}{b}\sqrt{2m\hat{J}_{fp}}\right) J_1^B\left(\frac{\pi\rho}{b}\right) \right\}^{\frac{1}{2}}. \quad (54)$$

and the half island amplitude is

$$\Delta \hat{J}_{max} = 2\sqrt{\frac{F}{G}} = \frac{1}{m}a^2 \sqrt{\frac{2}{3\xi} J_m^B(\frac{\pi}{b}\sqrt{2m\hat{J}}) J_1^B(\frac{\pi\rho}{b})}. \quad (55)$$

where the drift frequency near the center of the vortex is given by Eq. (18) in the dimensionless units with $\alpha = a$, and $\beta = 2b/\pi$:

$$\Omega_d \simeq \frac{\pi\gamma}{ab}. \quad (56)$$

We can now calculate the ratio of the sum of the two neighboring island widths and then apply the overlap criterion as in (29). An alternative procedure, which has been shown to be equivalent,¹³ is to calculate the island frequency, via (54) and then take the ratio to the next higher frequency, which in this case is Ω_d . The transition to large scale stochasticity in the neighborhood of the island is then given by

$$\frac{\Omega_I}{\Omega_d} \geq \frac{1}{6}. \quad (57)$$

Choosing parameters $a = 1.59$, $b = 7.5$, $m = 7$ and taking a drift orbit near the y-separatrix $R_s = \sqrt{2m\hat{J}_{fp}} = 7$ from Fig. 9 (calculated R_s value from Eq. (51) is smaller as $R_s = \sqrt{2m\hat{J}_{fp}} \approx 3.15$), we obtain $\frac{\Omega_I}{\Omega_d} = 0.12$. This value, in fact, underestimates the ratio, as the local value of Ω_d drops rapidly when approaching the separatrix. A more exact calculation near the separatrix can be performed, but requires more mathematical effort.¹³ We here simply note that the ratio obtained near the separatrix would satisfy (57) if the local value

of Ω_d were used. We can do the same calculation near the center of the vortex for $m = 5$, and $R_c = \sqrt{2m\hat{J}_{fp}} = 2$ taken from Fig. 9, to get $\frac{\Omega_L}{\Omega_D} = 0.02$. The message here is that it is easy to obtain stochasticity near the y-separatrix of the vortex potential structure but the orbits are mainly regular near the center of the vortex. Comparing these calculations with the numerical results shown in Fig. 9, we see that the five-island chain has little surrounding stochasticity, as expected. A significant factor left out in the drift frequency Ω_d and the fixed point J_{fp} calculations is finite gyroradius effects, which should give a critical value of velocity (or gyroradius) for the onset of stochasticity, as we see in Fig. 9.

8 Transport due to Ion Stochastic Motion

The calculation here is motivated by self-consistent simulation results from 2-d bounded magnetized codes which have indicated that there exists continuous particle transport in a cross-field plasma sheath with the large scale vortex potential structure. From dimensional considerations, an estimate of ion stochastic diffusion may be made. During a half gyromotion time $\pi\Omega^{-1}$, the particle is displaced over a distance $2\rho_i$, but the motion is correlated such that after a full gyroperiod it returns almost to its initial position but with a small displacement. If as a result of the ion gyromotion resonance with $\mathbf{E} \times \mathbf{B}$ drift motion, the ion motion becomes stochastic on this fast time scale, then the successive displacements are

independent. A estimate of the decorrelation scale length is an island size. With this scale length, which is that we used in Part I, the diffusion is

$$D_s \simeq \frac{L_I^2 \Omega_d}{2\pi}, \quad (58)$$

where L_I scales from the island action as

$$L_I^2 = 2m\Delta\hat{J}_{max} \quad (59)$$

Substituting Eqs. (55) into (59), and (59) and (56) into Eq. (58), we obtain

$$D_s \simeq \frac{a\gamma}{b} \sqrt{\frac{2}{3\xi} J_m^B \left(\frac{\pi}{b} \sqrt{2m\hat{J}} \right) J_1^B \left(\frac{\pi\rho}{b} \right)} \left(\frac{T_i}{eB} \right), \quad (60)$$

where we restore the dimensionality through the factor $\Omega\rho_i^2 = \frac{T_i}{eB}$. We compare this estimate with the numerically determined diffusion below. We emphasize here that it is hard to determine whether the scaling of D_s is Bohm-like in Eq. (60) since the parameters a, b, γ, ξ and ρ probably also change when the factor $\Omega\rho_i^2 = \frac{T_i}{eB}$ changes. We have extracted the dimensional units $\frac{T_i}{eB}$ for convenient comparison with the previous simulation studies by Theilhaber and Birdsall.³

In order to numerically calculate the convective diffusion coefficient, it is convenient to modify the potential well with two vortex structures as

$$\psi = \left\{ \left[\left(\frac{x - x_0}{a\rho_i} \right)^2 - \xi \left(\frac{x - x_0}{a\rho_i} \right)^4 \right] H(x) + \left[\left(\frac{x + x_0}{a\rho_i} \right)^2 - \xi \left(\frac{x + x_0}{a\rho_i} \right)^4 \right] H(-x) + \frac{1}{2} \left(1 - \cos \frac{\pi y}{b\rho_i} \right) \right\} \quad (61)$$

where H is the step function. The system is considered confined to a domain $-x_0 < x < x_0$ and $-y_0 < y < y_0$, where $x_0 = 2.5$ and $y_0 = b$. Beyond this domain, values in y are taken to be periodic. The particles leaving the boundaries at $x = \pm x_0$ are assumed to lost to the wall (hence, there is a sink) and reintroduced at $x=0$, Maxwellian distributed in velocity and y determined by energy conservation (hence, there is a source at $x=0$). When the system reaches a steady state, the strength of the source is obtained by counting the particles passing through $x = \pm x_0$. The particles are initially randomly distributed in the range $x = 0$ and $-y_0 < y < y_0$ and have a Maxwellian distribution in velocity with temperature T_i . Similar methods were previously used in calculation of effective diffusion in laminar convective flows²³ and for calculating the diffusion in standard mapping²⁴. By introducing a source at $x=0$, the effective diffusion coefficient is given by

$$D_{sp}^{sp} = S/\nabla^2 n \simeq S(2x_0)^2/N, \quad (62)$$

where N is the total number of particles in the simulation region $x > 0$ and S is the total number of particles entering at $x=0$ per unit time from boundary $x = x_0$.

In the numerical calculation, the system evolves for a few gyro-periods to reach a steady state. Without the vortex potential well, the particles are confined by magnetic field, and no particles diffuse to the wall. As the amplitude of potential increases, the loss of the particles increases. Figure 10(a) shows a plot of the number of particles reaching the wall

as a function of time for $\gamma = 2.5$. In this plot, 2500 particles were advanced for 500 gyro-periods. The total number of particles $n(t)$ escaping is plotted against t , and S is found to be $3\Omega^{-1}$. In this case, the numerical calculation of single particle trajectories found $D_s^{sp} = 0.03 \frac{T_i}{eB}$, which is in reasonable agreement with the theoretical estimate given by Eq. (60) $D_s^{th} = 0.023 \frac{T_i}{eB}$. In the theoretical calculation we have chosen $m = 7$ and taken a drift orbit near the y-separatrix $R_s = \sqrt{2m\hat{J}_{fp}} = 7$ from Fig. 9. Comparing these results to Theilhaber and Birdsall,³ they obtain $D_s^{th} = 0.04 \frac{T_i}{eB}$, is also in reasonable agreement with the results here. Again, we point out that the simulation used $\rho_i = 1$ and $v_{Ti} = 1$, so that the $\frac{T_i}{eB}$ scaling was not checked. Simulations with varying parameters could produce variations of $\frac{e\Phi_0}{T_i}$ and the size of the vortex in Eq. (60).

In comparing the properties of the surface of section plots given in Section 6 with the diffusion results, it is necessary to understand the qualitative features of the diffusive motion. In the surface of section plots, some particles lie on regular orbits inside the vortex well and other particles diffuse across the separatrix. In that case, we might expect that the density would be uniform in the interior of the vortex, because of the rapid drift motion, so that the global density would appear as a steep gradient confined to the separatrix layer. In this case, there would also be a hole in the particle scattering plot in $x - y$ space which is reserved for regular motion. Fig. 10(b) shows a instantaneous plot of density at

$t = 500\Omega^{-1}$. It is interesting to notice that the picture is quite different from that inferred above. The y-averaged density n varies linearly in x , vanishes at the position about one thermal ion gyroradius from the wall, as seen in Theilhaber and Birdsall simulation plots.³ This observation enables us to surmise that the motion is stochastic in the whole simulation region. This may be confirmed in the scattering plot of instantaneous particle position and velocity in Figs. 10(c)-(d). The particles near the center of the vortex, $|x - 2.5\rho_i| \leq 0.5\rho_i$, $|y| \leq 0.5\rho_i$, are found to have very high velocities $v \geq 3.0v_{T,i}$. The motion of particles at these high energies (very large ρ_i) most likely are stochastic and able to escape. The increase in kinetic energy of the particles near the bottom of the vortex well is a consequence of the stochastic motion, allowing individual particle to cross to lower potential regions. As the total particle energy is conserved, the consequence is an increase in kinetic energy and gyro-orbit size near the well center which maintains the stochasticity.

It is worth pointing out that during the simulation we observe that some particles are trapped near the source region. Thus, some fraction of the particles reintroduced at $x = 0$ as source particles have a chance to be trapped. But, compared with the stochastic flow, the relative number of trapped to escaping particles is small. By comparing particle scattering plots and y-averaged density plots at $t = 250\Omega^{-1}$ and $t = 1000\Omega^{-1}$, we confirm the approach to quasi-steady-state diffusive flow.

Finally, we note that the fully developed stochasticity in a single wave found in Part I, gives an estimate for the diffusion coefficient of $D_s \simeq 0.07 \frac{T_e}{eB}$. This is sufficient to allow electrons to diffuse across the sheath region at a rate equal to that of the fully developed ion diffusion to preserve ambipolarity.

9 Discussion and Conclusions

Particle simulation of motion in a plasma sheath with a magnetic field perpendicular to the electric field indicates there is quasi-steady-state consisting of vortex flow on the scale of the sheath dimension and a small amplitude wave spectrum with characteristic wavelength of the order of the ion gyroradius. There is a continuous transport of electrons and ions through this sheath, even in the absence of collisions, from the plasma source to the sink at the material wall.

We have investigated the mechanism for the transport by breaking up the problem into two non-self-consistent parts, and showing that they can combine to transport both ions and electrons across the sheath. The primary driving mechanism is the resonance interaction of harmonics of the vortex frequency with the ion gyrofrequency which leads to stochastic diffusion. For the parameters of the vortex size and strength, and the self-consistent ion temperature, the numerical integrations of single particles in this field shows

that the stochastic motion transports ions across the sheath at a rate in good agreement with that found in the simulation.

Because time and space scales are not well separated, analytic techniques using secular perturbation theory are not sufficiently accurate to quantitatively calculate the stochasticity and resultant diffusion. They do, however, uncover the basic mechanisms of island formulation and destruction, which are illustrated by surface of section plots of the single particle motion. Simple analytic estimates of the diffusion rate, employing the concepts of diffusion theory from situations in which the scales are better separated, give reasonable estimates of the transport rate.

We expect that the stochastic ion motion and the resulting interception of ion orbits with walls would lead to macroscopic charge fluctuation that generate a wave spectrum. Indeed these charge fluctuations and waves are seen in the simulation. Without inquiring into the details of the spectrum, we show that even a single wave, of the frequency and wave number corresponding to the peak observed amplitude, is sufficient to resonate with the $\mathbf{E} \times \mathbf{B}$ motion of the electrons in the vortex to generate large scale stochasticity. Additional waves, at the same overall amplitude level, tend to make the stochasticity more uniform with the same general rate of transport. For $\mathbf{E} \times \mathbf{B}$ motion with one single small amplitude wave there is better quantitative comparison of the analytic methods with the single particle

numerical integrations. This is because the wave frequency is a true constant of motion which made the system well suited for the analytic methods used. We have presented these comparisons and shown the agreement to be reasonable. The transport rate is found to be sufficient to account for electron loss at the same rate as the ions, and thus no additional ambipolar effects need be postulated.

The parameters explored in our study were chosen with the guidance of the simulations, in which these parameters were self-consistently generated. Significant reduction of the self-consistent perturbation parameters or of the gyroradius led to considerably less stochasticity and consequently less diffusion. This also may give additional insight into the self-consistent problem, as it indicates that the wave strength builds up until ambipolarity is just satisfied.

The fact that our scaling with $\frac{T_i}{eB}$ (ρ_i and v_{Ti}) in Eq. (60) is only Bohm-like for fixed $\frac{e\Phi_0}{T_i}$, $\frac{\rho_i}{b}$, and $\frac{a}{b}$, does not mean that an investigation of the scaling in the simulation would not give Bohm-like results; i.e., as parameters T_i and B change in the simulation, quantities $\frac{e\Phi_0}{T_i}$, a and b (the ratios of the vortex size to the gyro-radius) could either remain constant or change in such a way that Eq. (60) would give the Bohm-like diffusion. Our work points out the need for simulations for a wide parameter range, in order to investigate the scaling, which could then be compared to the type of calculation we have performed.

The treatment used in this study to determine the transport mechanism and calculate

the rate of diffusive loss across the sheath region is not self consistent. In fact it is our ability to independently vary certain parameters and investigate the consequence of the variation that gives us insight into the transport mechanism. Nevertheless, even within the conceptual framework of our study, there is a step that has been left out, the determination of the waves that drive the electron transport. An approach to this problem is a non-self-consistent Fourier analysis of the ion charge fluctuations within the context of ion stochastic motion and transport. However, since the fluctuations can both affect the ion motion and be affected by the electron motion, it is not clear that the resultant fluctuation spectrum will closely approximate the self-consistent one. In any case, such a study takes us beyond the framework of this paper, and we leave it for future work.

Acknowledgments

We thank Dr. Kim Theilhaber for enlightening discussions on his cross field sheath simulations. This work was performed at the University of California at Berkeley under U.S. Department of Energy contract DE-FG03-90ER54079, U. S. Office of Naval Research Contract N00014-89-J-1097, and N00014-90-J-1198, and National Science Foundation Grant ECS 8910762. This research was also supported in part by an appointment (S.P.) to the U.S. D.O.E. Fusion Energy Postdoctoral Research Program administered by Oak Ridge

References

1. K. Theilhaber and C.K. Birdsall, *Phys. Rev. Lett.* **62**, 772 (1989).
2. K. Theilhaber and C.K. Birdsall, *Phys. Fluids B* **1**, 2241 (1989).
3. K. Theilhaber and C.K. Birdsall, *Phys. Fluids B* **1**, 2260 (1989).
4. W. Horton, T. Tajima, and T. Kamimura, *Phys. Fluids* **30**, 3485 (1987).
5. T. Tajima, W. Horton, P. J. Morrison, J. Schutkeker, T. Kamimura, K. Mima, and Y. Abe, *Phys. Fluids B* **3**, 938 (1991).
6. B. V. Chirikov, *Plasma Phys.* **1**, 253 (1960).
7. R. H. Cohen, G. Rowlands and J. H. Foote, *Phys. Fluids* **21**, 627 (1978).
8. F. Jaeger, A. J. Lichtenberg, and M. A. Lieberman, *Plasma Phys.* **14**, 1073 (1972).
9. M. A. Lieberman and A. J. Lichtenberg, *Plasma Phys.* **15**, 125 (1973).
10. C.F.F. Karney, *Phys. Fluids* **21**, 1584 (1978).
11. G.R. Smith and A.N. Kaufman, *Phys. Fluids* **21**, 2230 (1978).
12. B.V. Chirikov, *Phys. Rep.* **52**, 263 (1988).

13. A.J. Lichtenberg and M.A. Lieberman, *Regular and Stochastic Motion* (Springer, Berlin, 1983).
14. M. Brambilla and A. J. Lichtenberg, *Nuclear Fusion* **13**, 517 (1973)
15. W. M. Nevins, J. Harte and Y. Gell, *Phys. Fluids* **22**, 2108 (1979).
16. W. Horton, *Plasma Phys.* **27**, 937 (1985).
17. M. Pettini, *et al*, *Phys. Rev. A* **38**, 344 (1988).
18. A.R. Osborne and R. Caponio, *Phys. Rev. Lett.* **64**, 1733 (1990).
19. R. E. Waltz, *Phys. Fluids* **26**, 169 (1983).
20. C.W. Gear, *Numerical Value Problems in Ordinary Differential Equations*, (Prentice-Hall, Englewood Cliffs, N.J., 1971).
21. I. Doxas, W. Horton, and H. L. Berk, *Phys. Fluids A* **2**, 1906 (1990).
22. C. K. Birdsall and A. B. Langdon, **Plasma Physics via Computer Simulation**, (McGraw-Hill, New York, 1985).
23. M. N. Rosenbluth, H. L. Berk, I. Doxas, and W. Horton, *Phys. Fluids* **30**, 2636 (1987).
24. N. W. Murray, M. A. Lieberman, and A. J. Lichtenberg, *Phys. Rev. A* **32**, 2431 (1985).

Figures

Figure 1: Characterization of the physical system of interest. A large scale coherent circular flow (or vortex) interacting with small amplitude traveling waves.

Figure 2: Contours of the potential, Eq. (4) with $\psi(u) = e^{-\frac{1}{2}u}$, with $B = 1$, $\gamma = 2.5$, $\alpha = 1.25$, $\beta = 3.83$, $v_{00} = 0.5v_{Ti}$, $\rho_i/L_s = 0$, and $k\rho_i = 3.83$. These parameters are chosen to compare to the results in Refs. 2 and 3.

Figure 3: Plot of (x, y) when $\tilde{\omega}_1 t = 2\pi n$, $n = 1, 2, 3, \dots$ (a) $\epsilon = 0.015$, (b) $\epsilon = 0.02$.

Figure 4: Action angle coordinate surface of section plot for the $\epsilon = 0.015$ case. Plot of (J_0, θ_0) when $\tilde{\omega}_1 t = 2\pi n$, $n = 1, 2, 3, \dots$

Figure 5: Surface of section plot with four waves. Plot of (x, y) when $\tilde{\omega}_4 t = 2\pi n$, $n = 1, 2, 3, \dots$

Figure 6: Four test particle orbits are shown just at the interior edge of the vortex with velocity shear $\delta = 0.015$.

Figure 7:(a) Perspective plot of the potential surface, Eq. (43) with $\frac{\epsilon\Phi}{T_i} = \gamma\psi = \gamma[(\frac{x}{a\rho_i})^2 - \xi(\frac{x}{a\rho_i})^4 + \frac{1}{2}(1 - \cos \frac{\pi y}{b\rho_i})]$ with $\gamma = \frac{\epsilon\Phi_0}{T_i} = 2.5$, $a = 1.59$, $b = 7.5$ and $\xi = 0.17$.
(b) contour plot of $\psi(x, y)$ in (a).

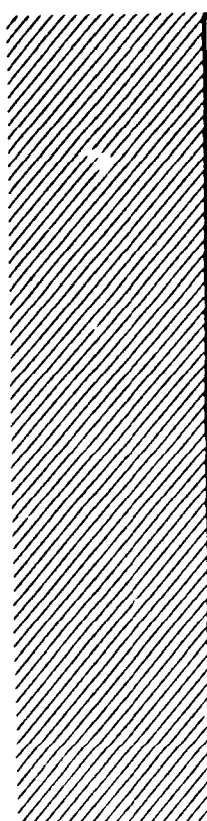
Figure 8: Plots for potential, Eq. (42). The vortex center is located at $x = 0$ and $y = 0$. (a) Surface of section for $N=12$ particles, $r_0 = 1\rho_i$, $v_{00} = 0.71v_{Ti}$ and $\gamma = 2.5$; (b) Single particle orbit for one set of the 4-islands in (a).

Figure 9: Plots for potential, Eq. (43). The vortex center is located at $x = 0$ and $y = 0$. (a) Surface of section for $N = 20$ particles, $r_0 = 0.5\rho_i$, $v_{00} = 1.55v_{Ti}$, and $\gamma = 2.5$; (b) Surface of section for $N = 20$ particles, $r_0 = 0.5\rho_i$, $v_{00} = 1.7v_{Ti}$, and $\gamma = 2.5$.

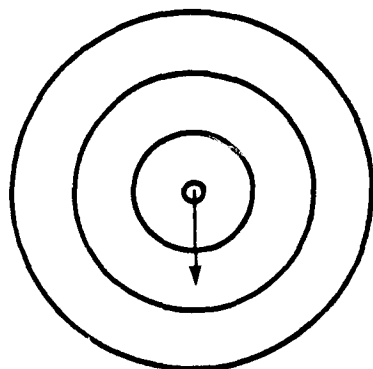
Figure 10: Typical plots for diffusion measurement. The vortex center is located at $x_0 = 2.5\rho_i$, $y = 0$, the source at $x = 0$ and the sink at $x = 5.0\rho_i$. Here, 2500 particles are advanced in time by $500\Omega^{-1}$. (a) Number of particles N , escaping the region $|z| > 2x_0$ plotted against time t . Instantaneous plots at $t = 500\Omega^{-1}$: (b) Profile of the y-averaged ion density; (c) ion scatter plot; (d) ion velocity plot.

WALL, $\phi = 0$

SMALL AMPLITUDE WAVES



VORTEX, OR
POTENTIAL WELL



$$\frac{e\phi}{T_i} \approx -2.5$$

$$\Delta x \approx 5\pi$$

$$\Delta y \approx 15\pi$$

$$\frac{e\phi}{T_i} \ll 1$$

$$k\rho_j \approx 1$$

$$\omega/\omega_{ci} \approx 1$$

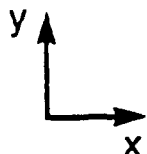


FIGURE 1

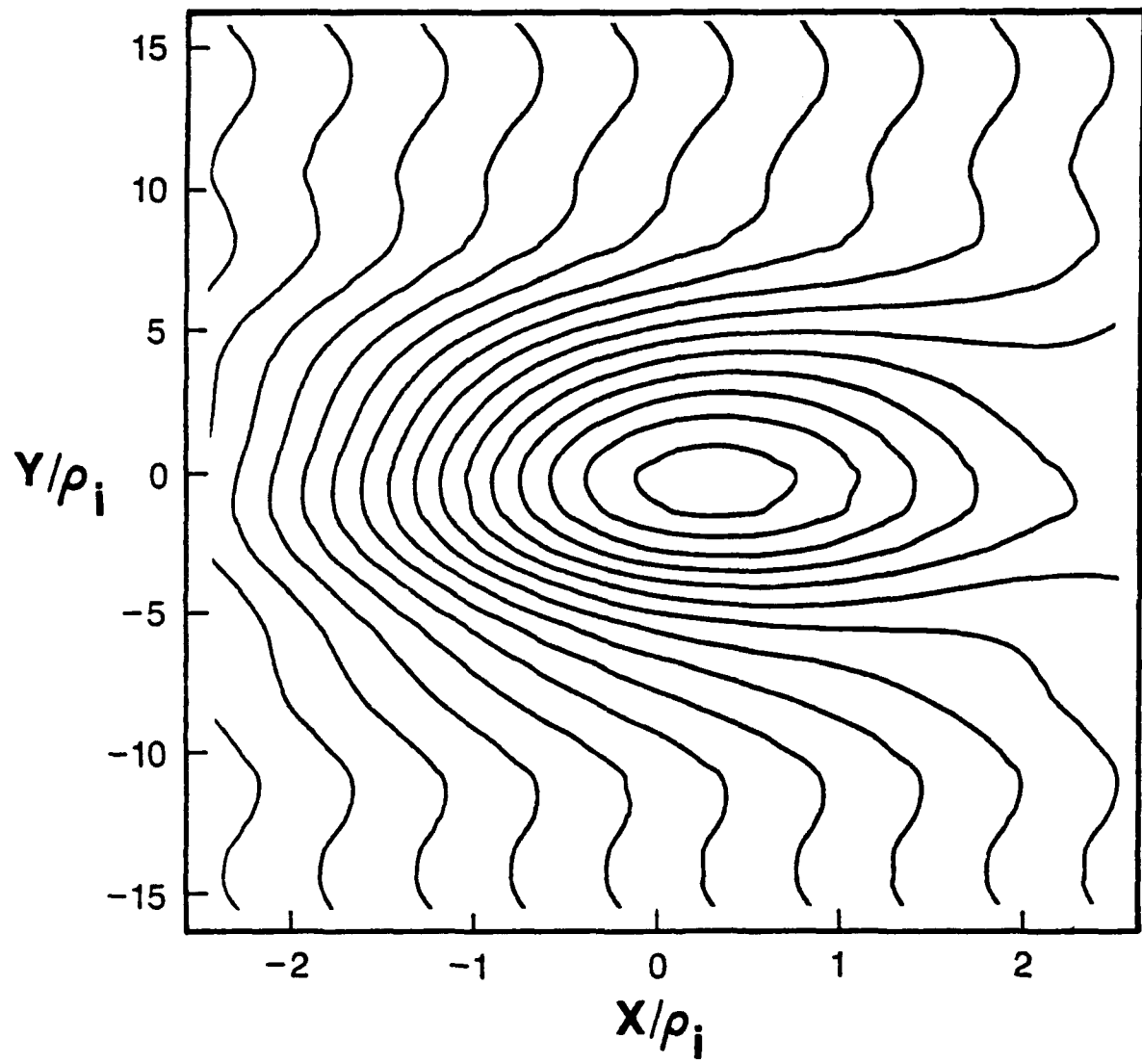


FIGURE 2

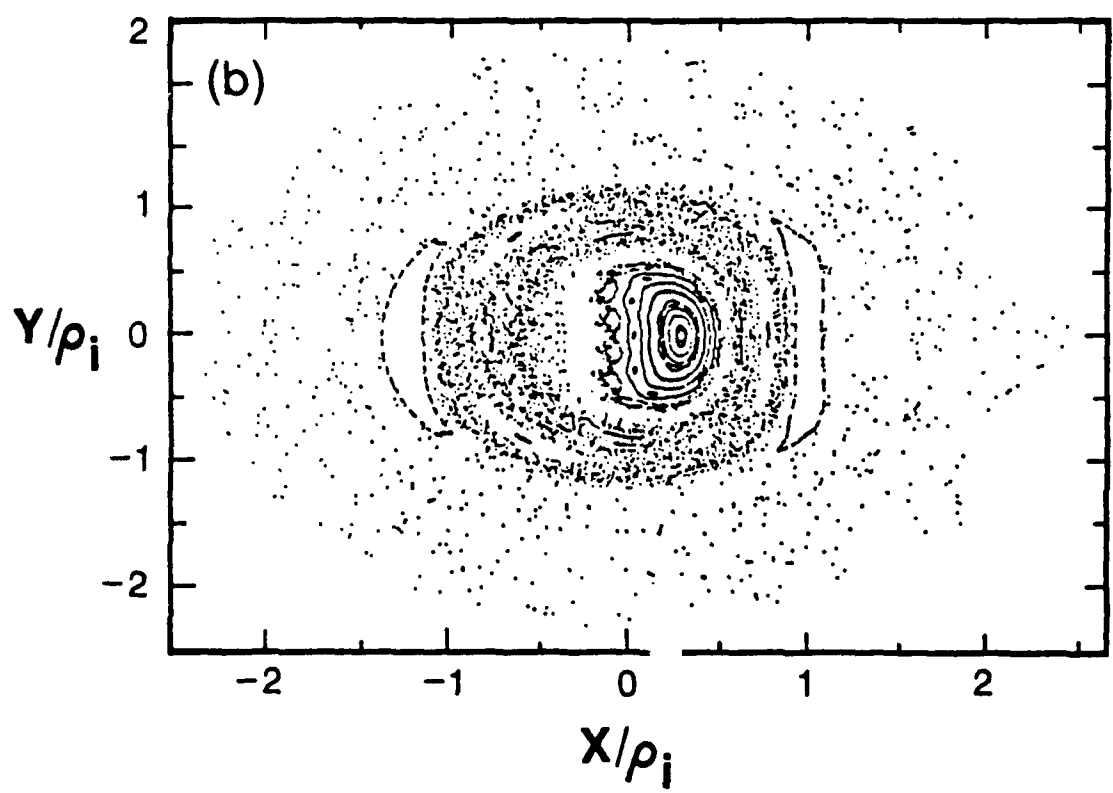
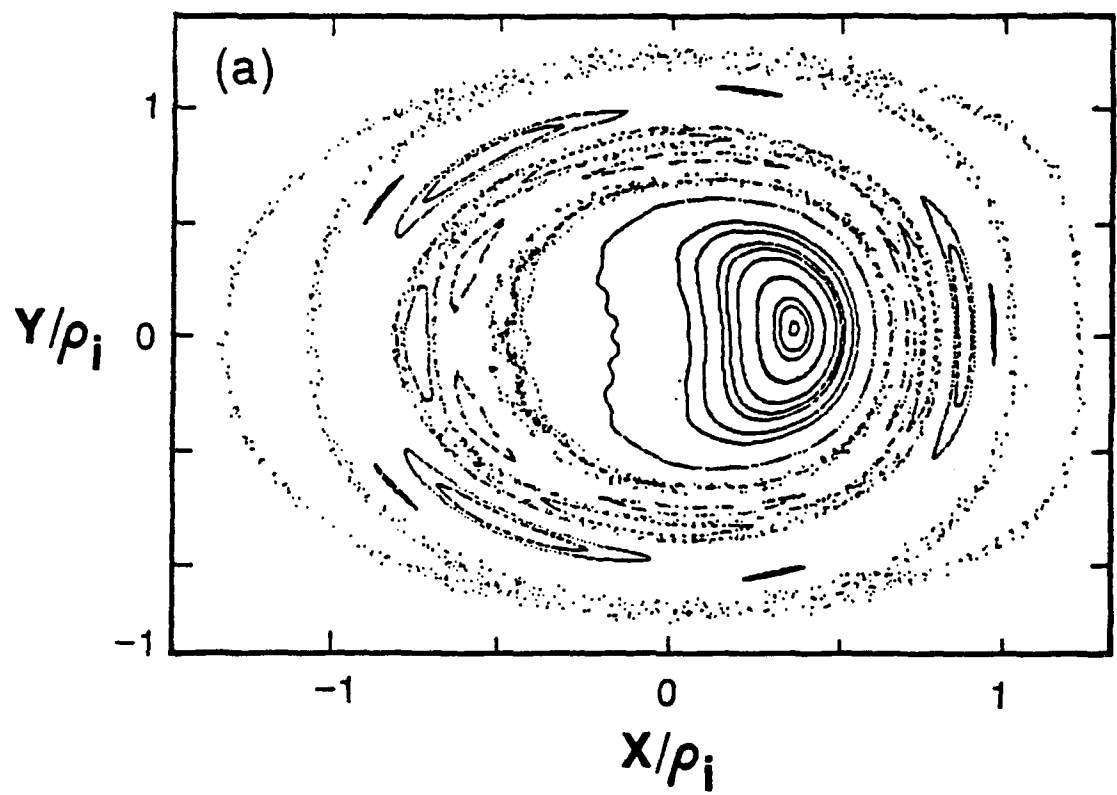


FIGURE 3

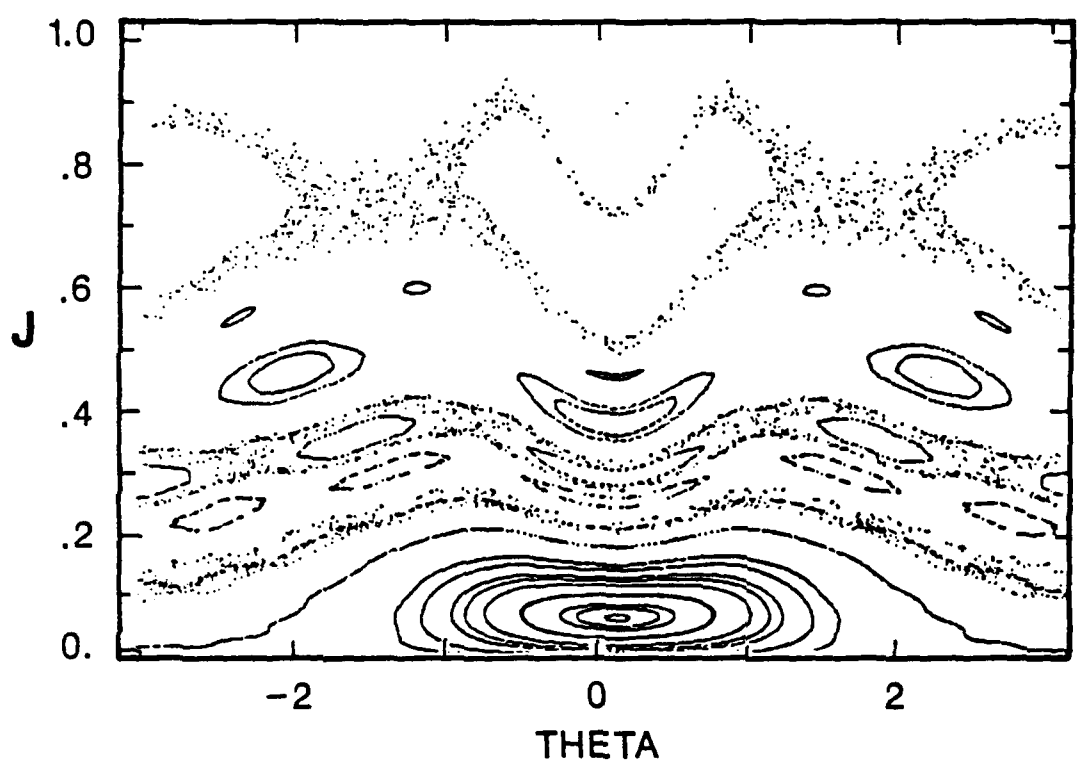


FIGURE 4

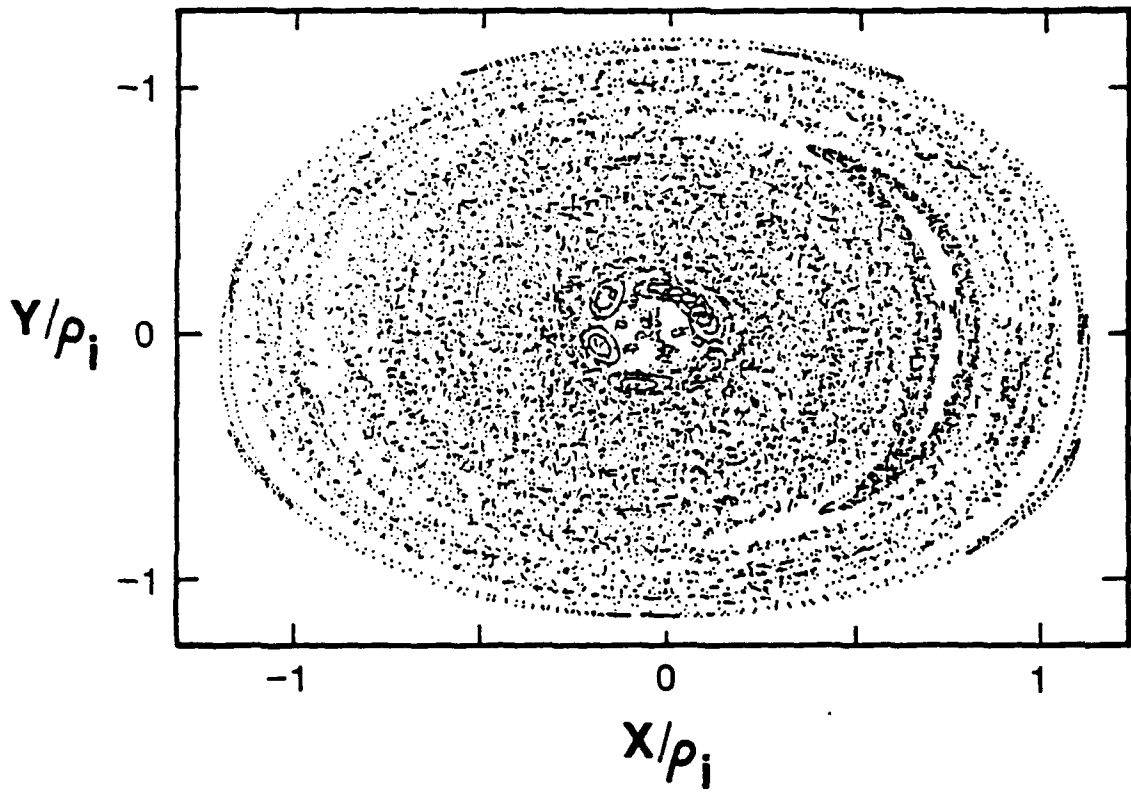


FIGURE 5

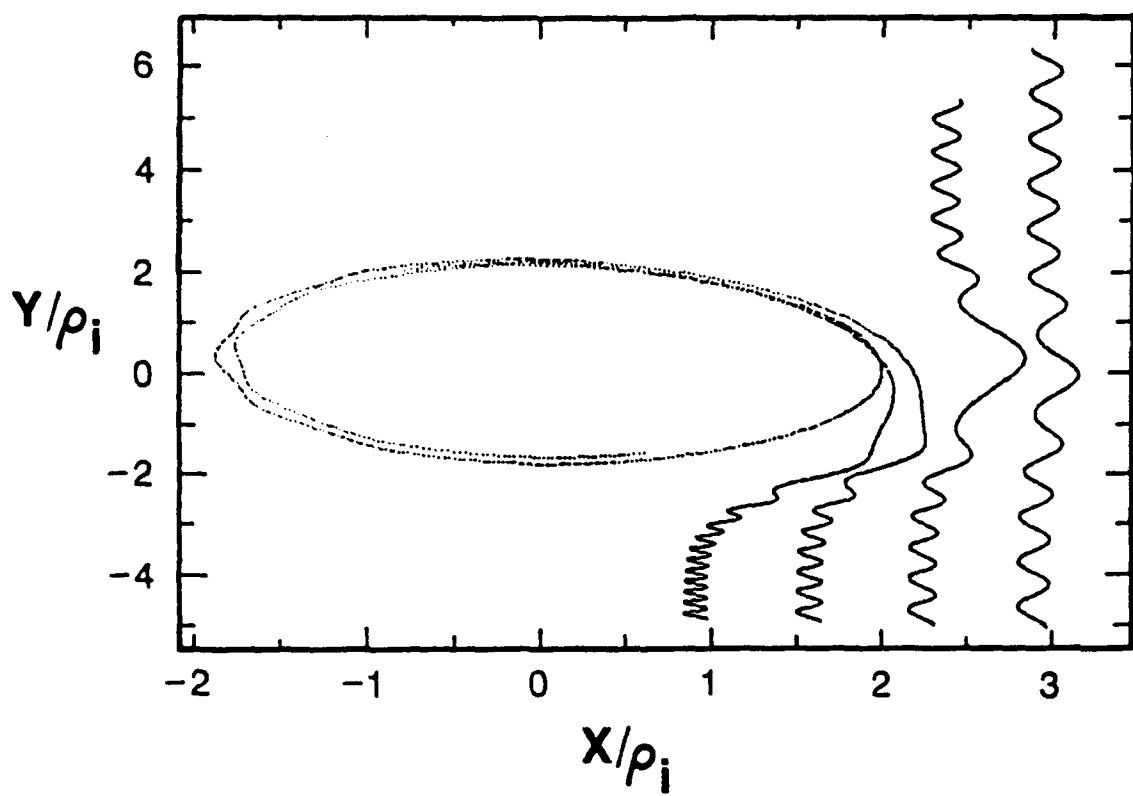


FIGURE 6

A SURFACE PLOT OF ϕ

(a)

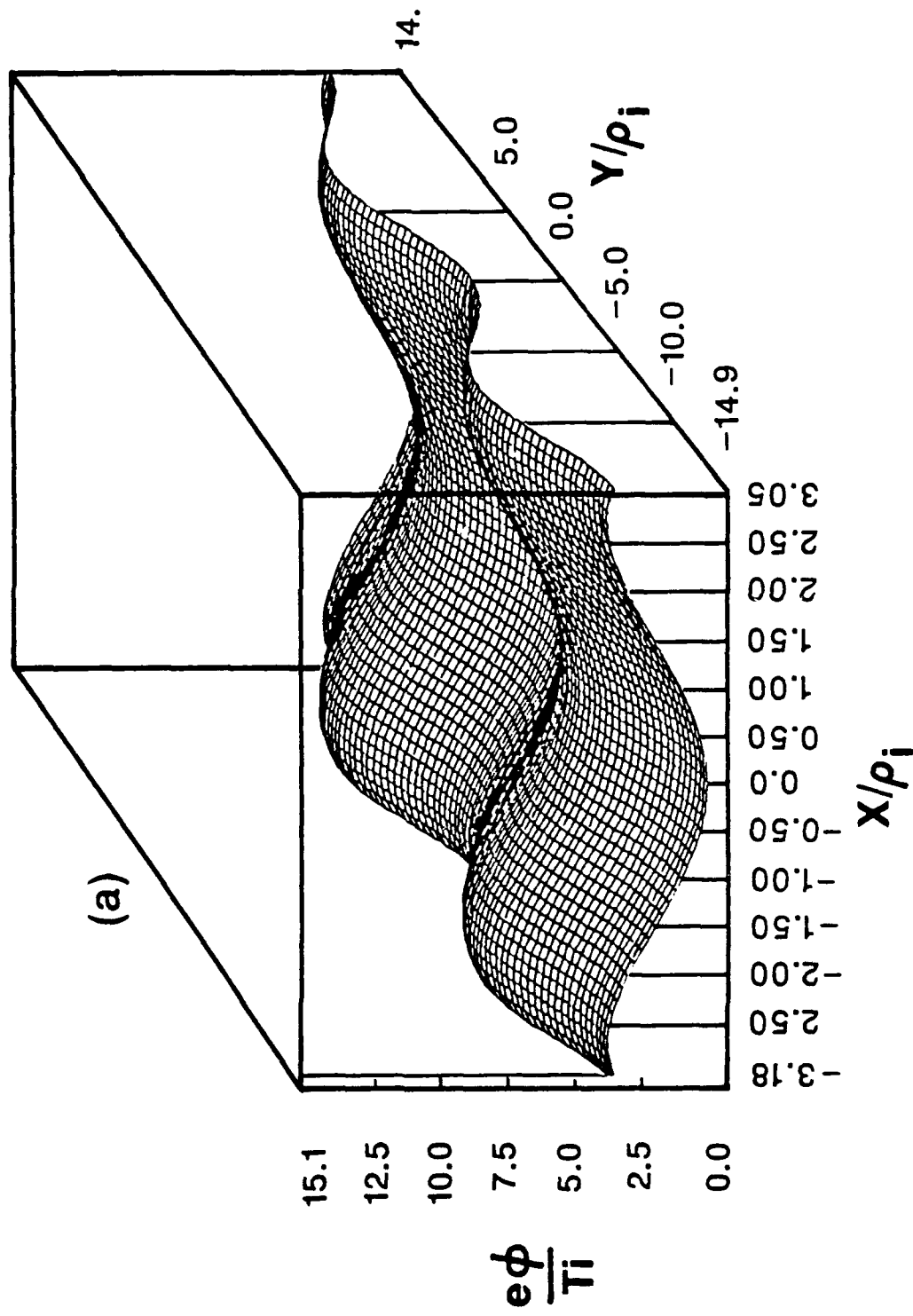


FIGURE 7 (a)

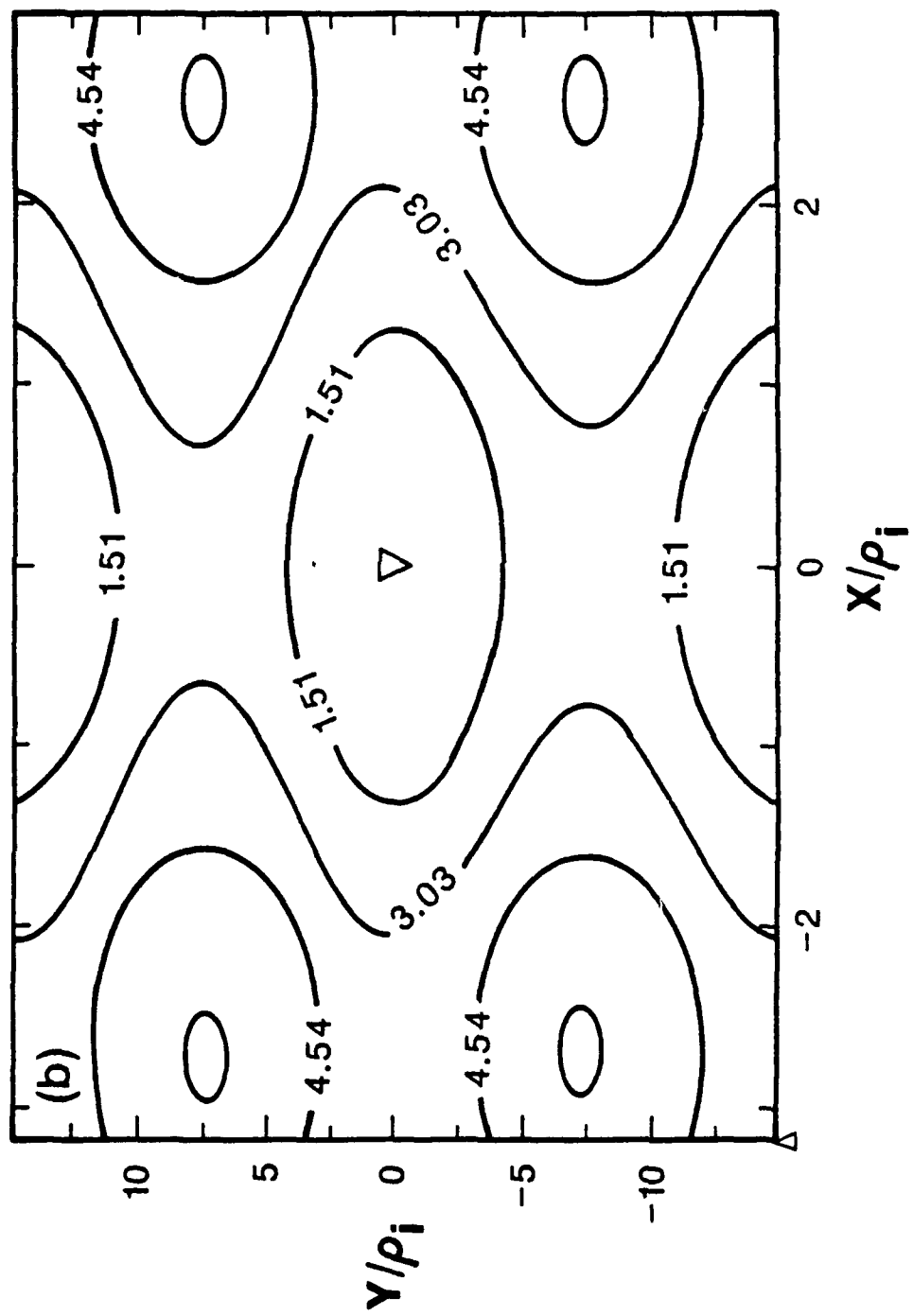


FIGURE 7 (b)

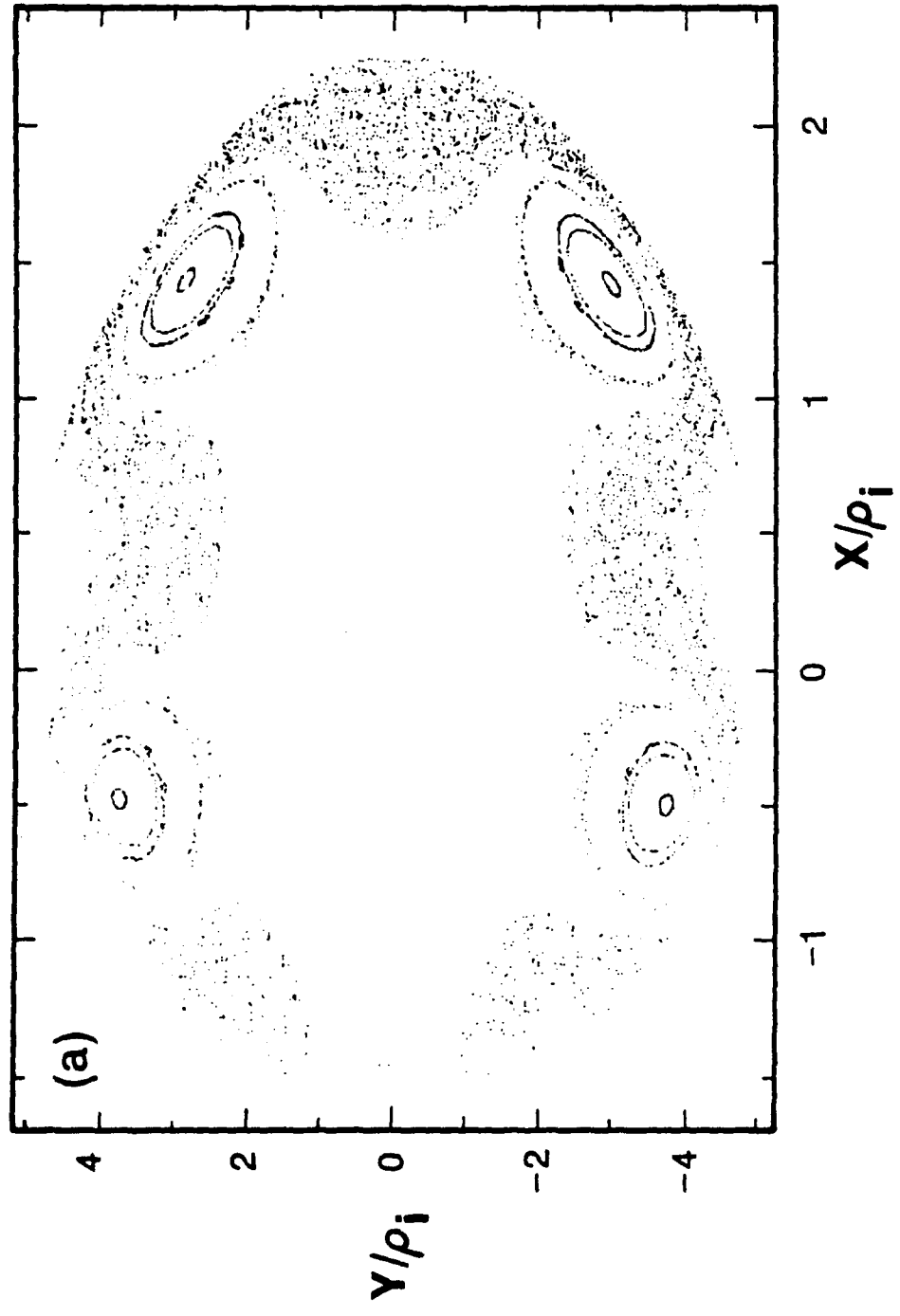
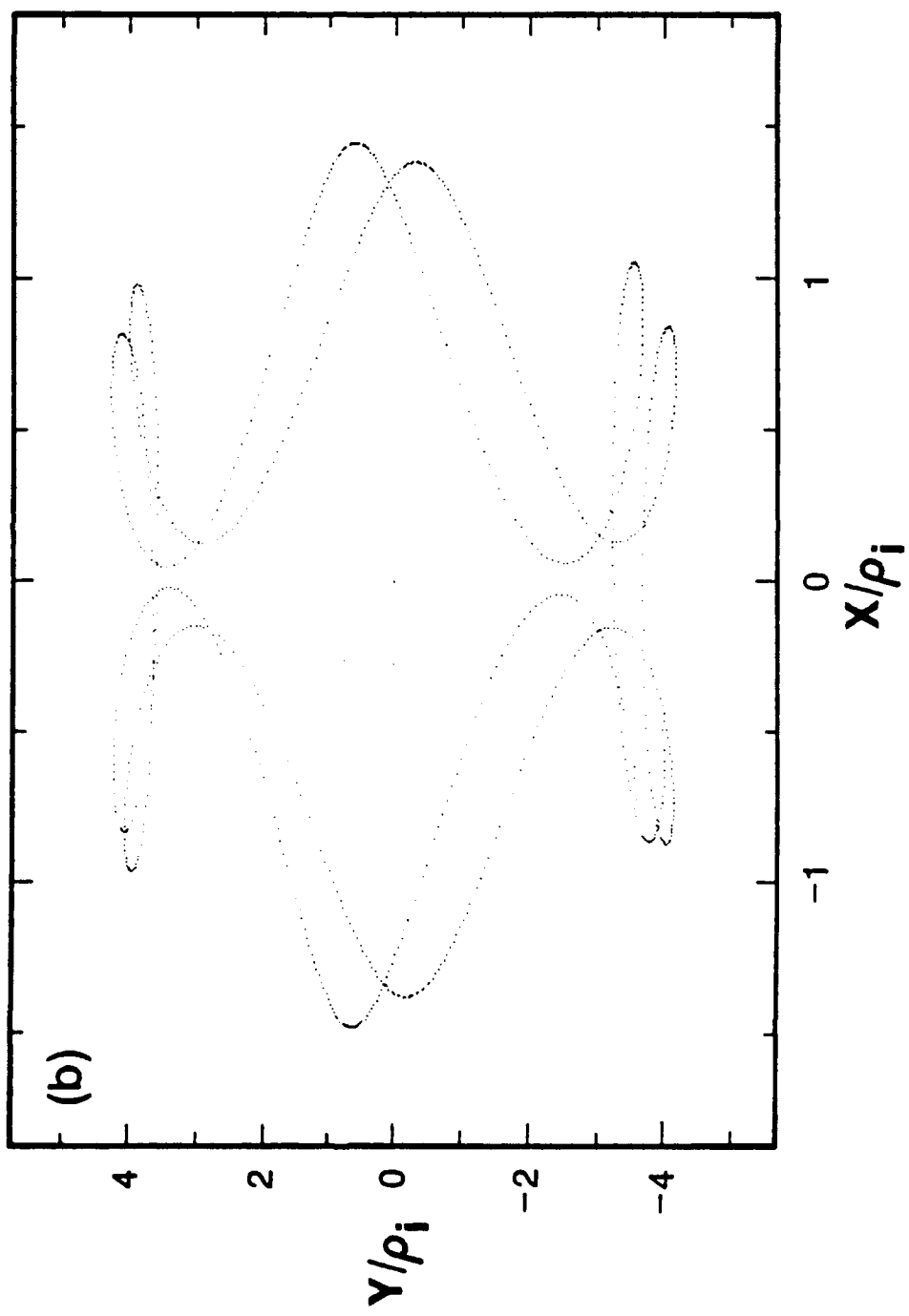


FIGURE 8 (a)

FIGURE 8 (b)



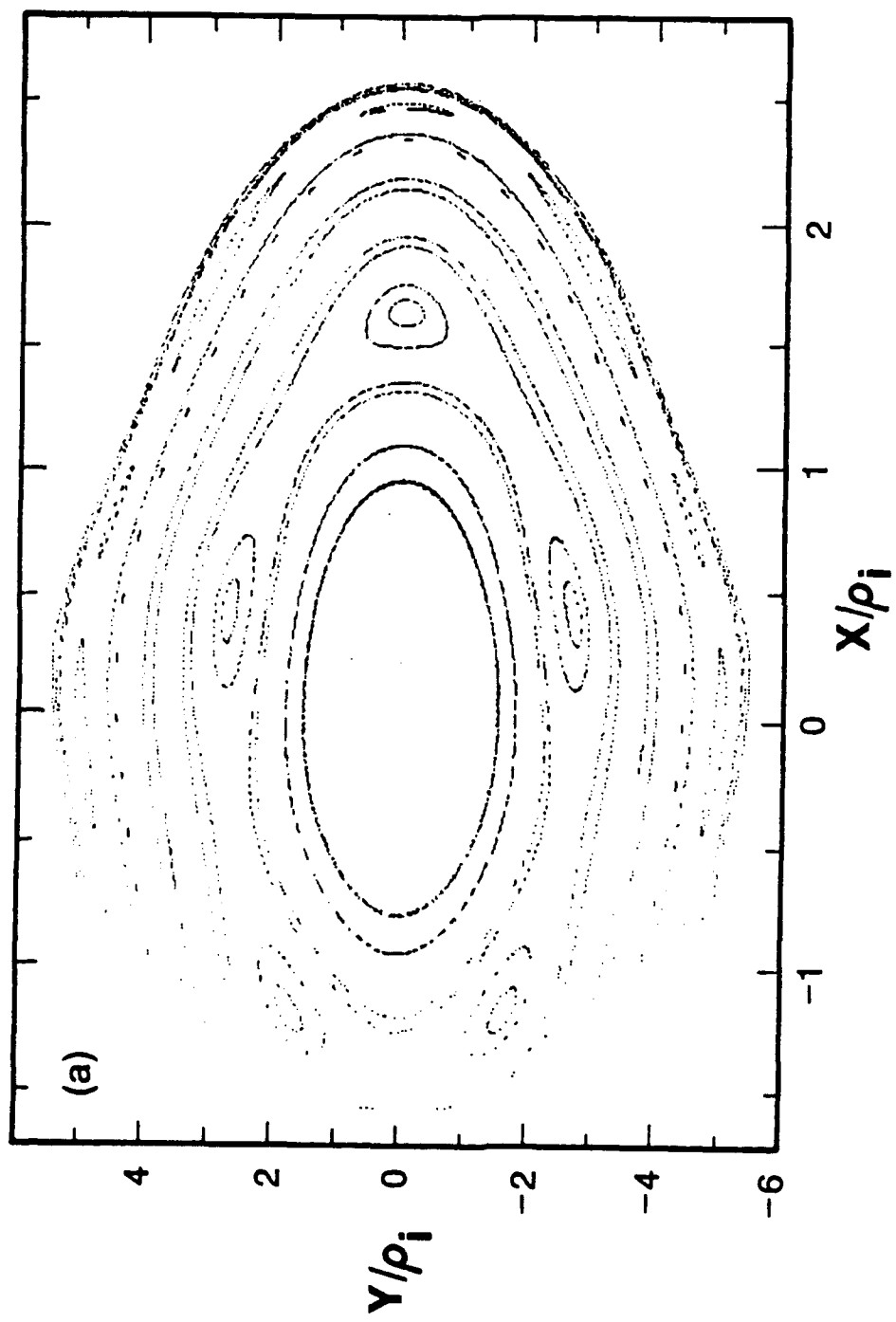


FIGURE 9 (a)

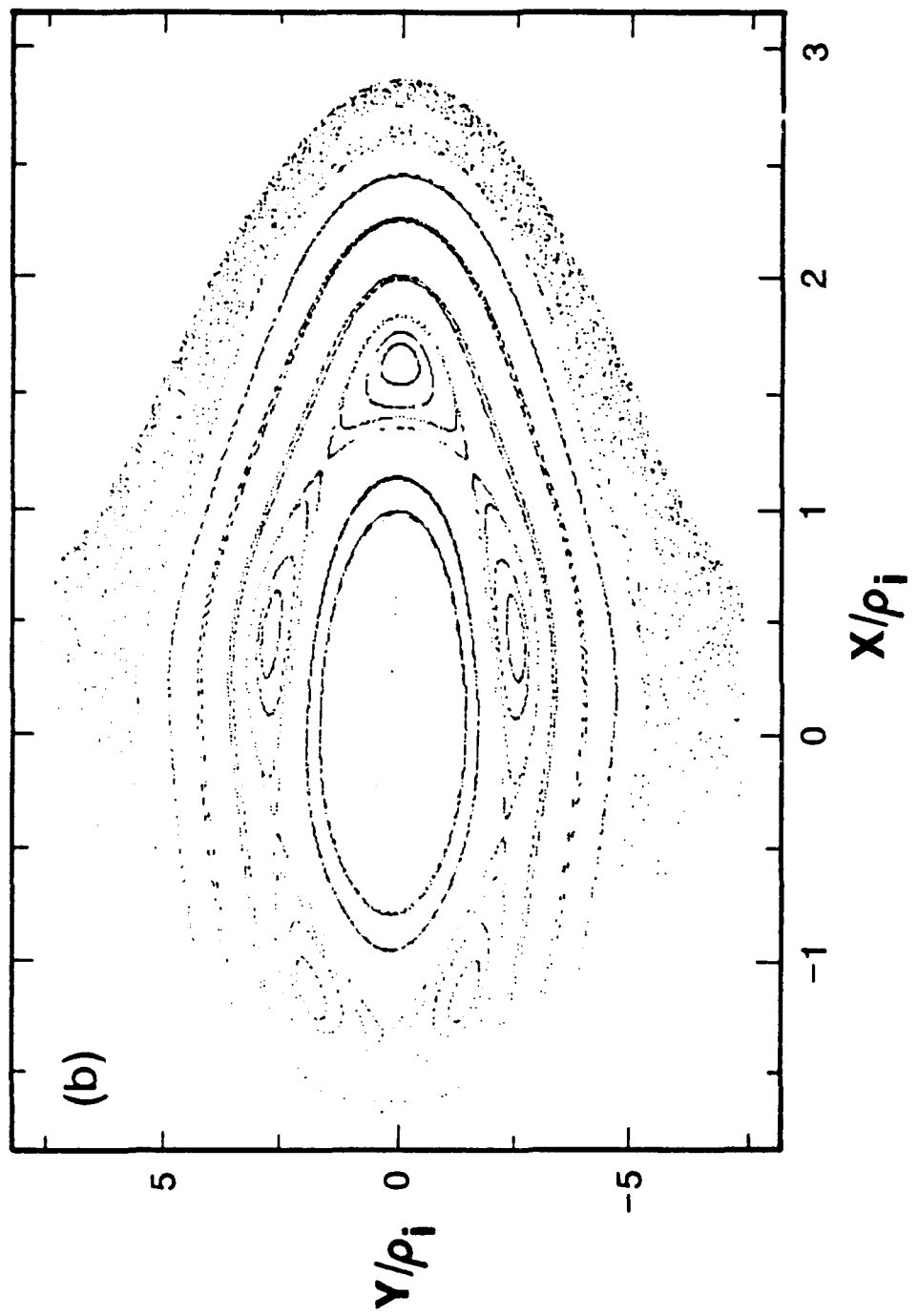


FIGURE 9 (b)

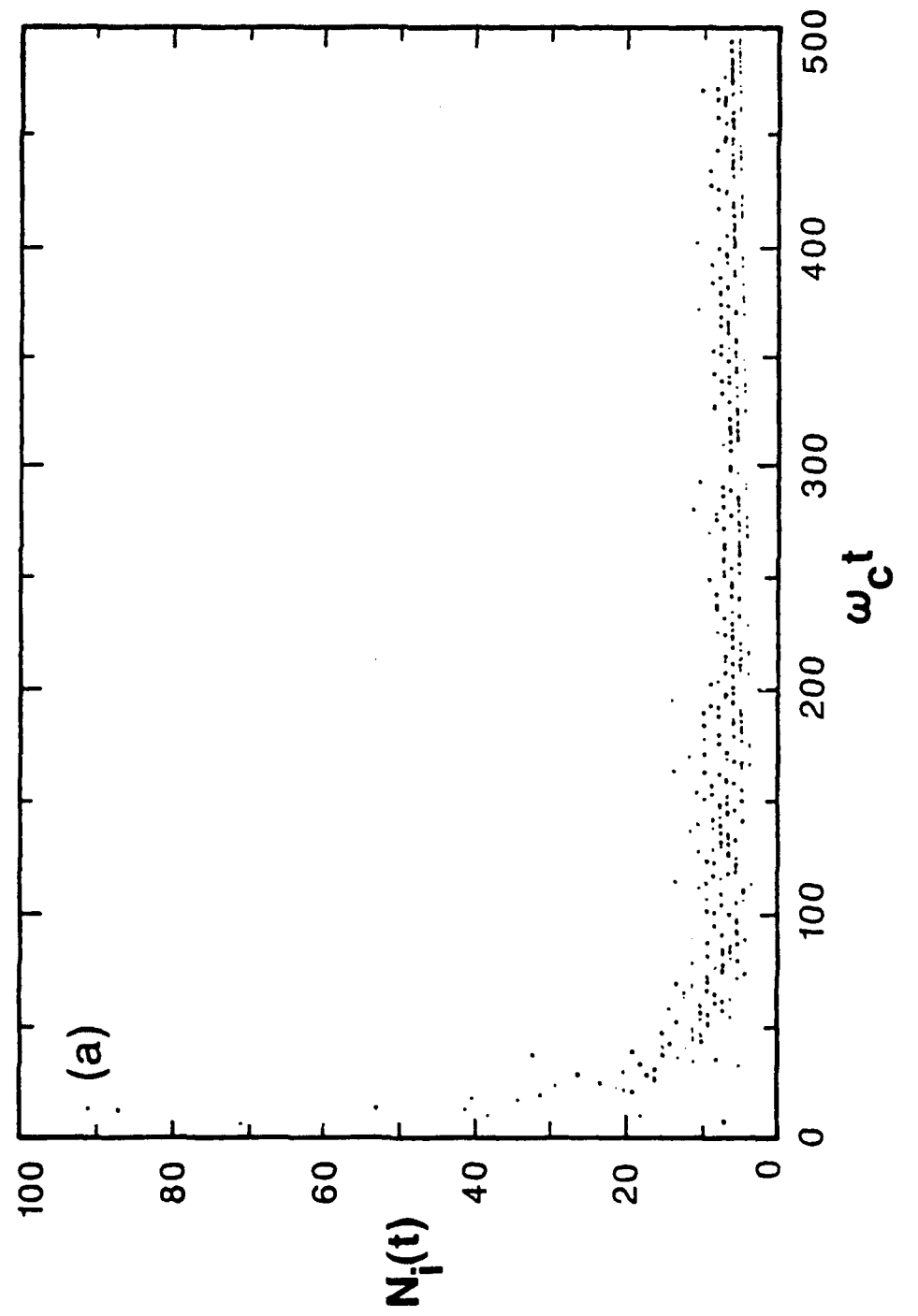
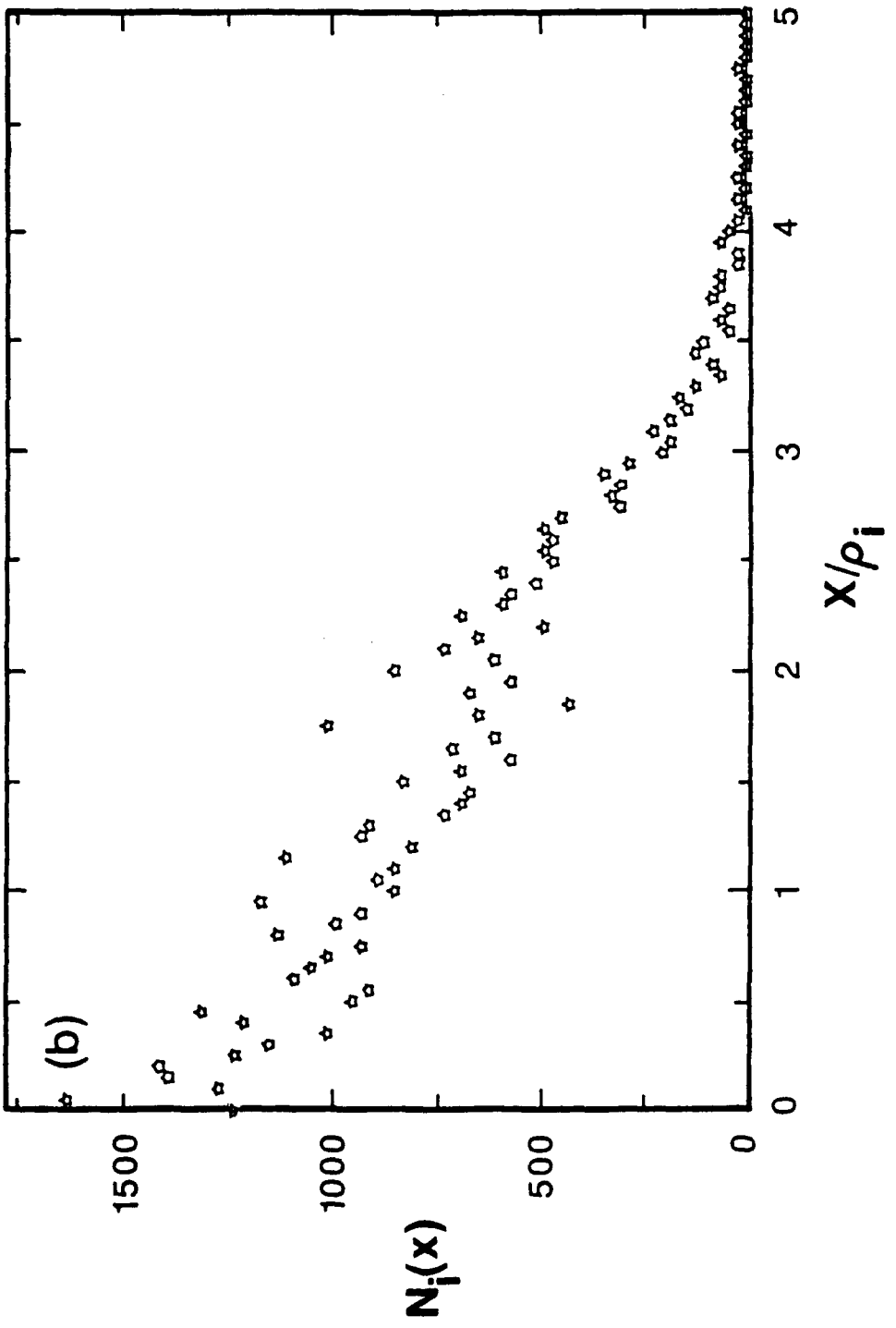


FIGURE 10 (a)

FIGURE 10 (b)



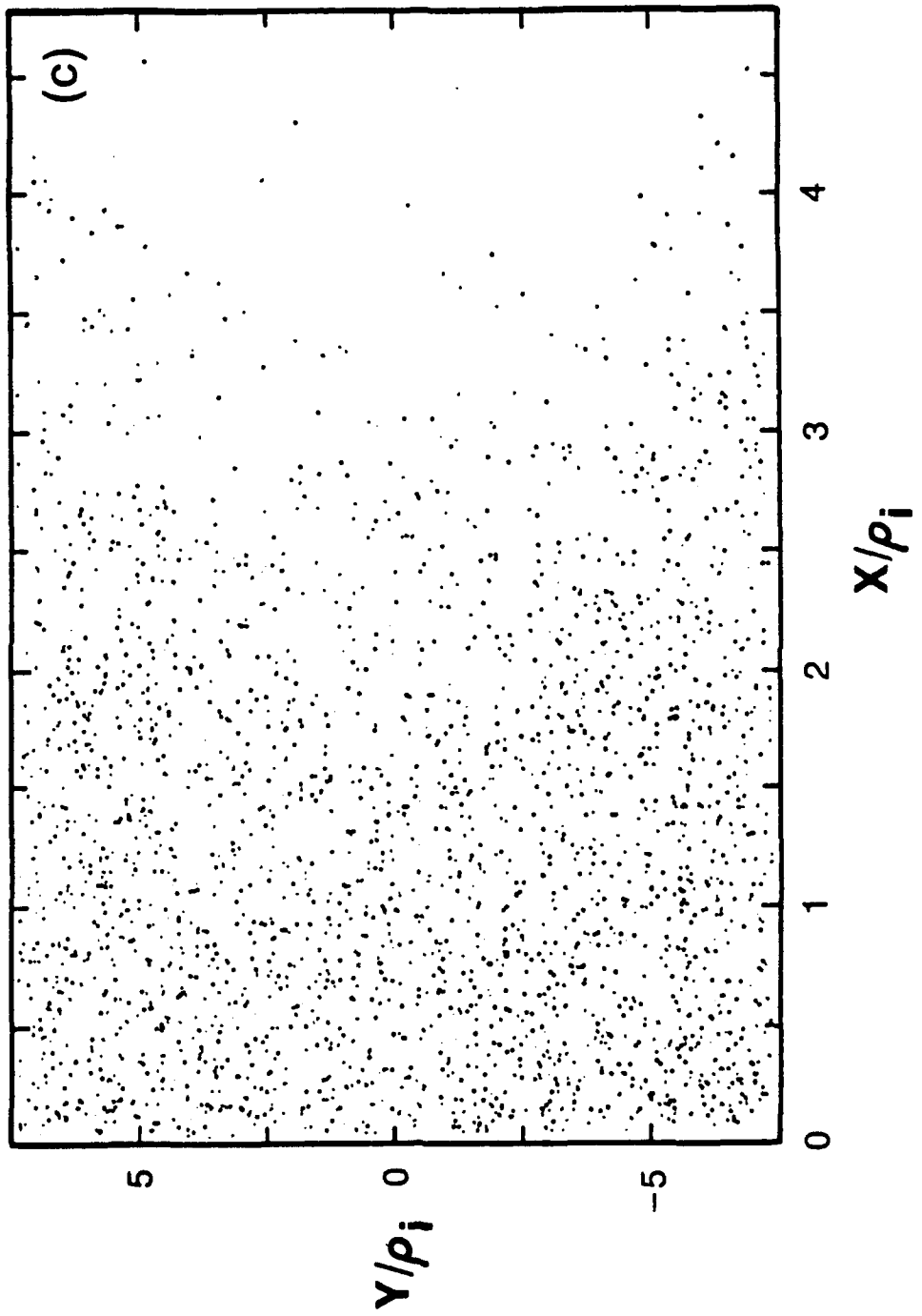


FIGURE 10 (c)

FIGURE 10 (d)

